JOURNAL OF GEOPHYSICAL RESEARCH, VOL. 113, C01018, doi:10.1029/2006JC003976, 2008

Click Here for Full Article

The path-density distribution of oceanic surface-to-surface transport

Mark Holzer[1,2,3,4] and François W. Primeau[5]

Received 18 October 2006; revised 10 August 2007; accepted 8 October 2007; published 24 January 2008.

[1] A novel diagnostic for advective-diffusive surface-to-surface paths is developed and applied to a global ocean model. The diagnostic provides, for the first time, a rigorous quantitative assessment of the great ocean conveyor's deep branch. A new picture emerges of a diffusive conveyor in which the deep North Pacific is a holding pen of long-residence-time water. Our diagnostic is the joint density, η, per unit volume and interior residence time, τ, of paths connecting two specified surface patches. The spatially integrated η determines the residence-time partitioned flux and volume of water in transit from entry to exit patch. We focus on interbasin paths from high-latitude water mass formation regions to key regions of re-exposure to the atmosphere. For non-overlapping patches, a characteristic timescale is provided by the residence time, τ_ϕ, for which the associated flux distribution, ϕ, has its maximum. Paths that are fast compared to τ_ϕ are organized by the major current systems, while paths that are slow compared to τ_ϕ are dominated by eddy diffusion. Because ϕ has substantial weight in its tail for $\tau > \tau_\phi$, the fast paths account for only a minority of the formation-to-re-exposure flux. This conclusion is expected to apply to the real ocean based on recent tracer data analyses, which point to long eddy-diffusive tails in the ocean's transit-time distributions. The long-τ asymptotic path density is governed by two time-invariant patterns. One pattern, which we call the Deep North Pacific pattern, ultimately dominates a secondary redistribution pattern.

Citation: Holzer, M., and F. W. Primeau (2008), The path-density distribution of oceanic surface-to-surface transport, *J. Geophys. Res.*, *113*, C01018, doi:10.1029/2006JC003976.

1. Introduction

[2] Oceanic surface-to-surface transport is of fundamental importance for understanding the ocean's role in sequestering and redistributing tracers of atmospheric origin, as well as heat and fresh water. Fluid elements that are transported from the mixed layer into the permanent thermocline carry with them the mixed-layer tracer concentrations at the location of their last contact with the mixed layer. In the absence of interior sources, we may think of individual fluid elements retaining their tracer labels until they re-enter the mixed layer, so that interior concentrations are determined by the advective-diffusive transport paths of these fluid elements. In a coarse-grained description of the circulation, implicit in essentially all global models, eddy diffusion due to quasi-random turbulent motions and shear dispersion is an important contributor to the transport and redistribution of fluid elements. The effects of such eddy diffusion cannot be captured by transport diagnostics like the overturning stream function, which are based solely on the explicitly resolved velocity field.

[3] Recent work has attempted to use Lagrangian particles in coarse-resolution ocean models to trace out the upper branch of the ocean's conveyor circulation [*Drijfhout et al.*, 1996; *Speich et al.*, 2001]. Studies with time-averaged eddy-permitting models [e.g., *Drijfhout et al.*, 2003] explicitly calculate the effect of eddy correlations between velocity and isopycnal thickness. *Sun and Bleck* [2001] define flux tubes for the ocean's mass flux to trace out circulation paths using an isopycnal Eulerian model. However, none of these studies accounts for the effectively diffusive transport of isopycnal turbulence, and the Lagrangian calculations additionally neglect cross-isopycnal diffusive fluxes.

[4] In this paper we construct a new transport diagnostic for tracking the combined advective and eddy-diffusive surface-to-surface transport of fluid elements. The diagnostic $\eta(\mathbf{r}, \tau, \Omega_i, \Omega_f; t)\, d^3r\, d\tau$ is the fraction of water in the volume element d^3r at point $\mathbf{r}$ and time t that was last ventilated on surface patch Ω_i and is destined to be re-exposed to the atmosphere on patch Ω_f after residing in the ocean interior for a time $\tau \in (\tau, \tau + d\tau)$. Because each fluid element that makes the $\Omega_i \rightarrow \Omega_f$ trip is tracing out an $\Omega_i \rightarrow$

---

[1] Department of Applied Physics and Applied Mathematics, Columbia University, New York, New York, USA.

[2] Also at NASA Goddard Institute for Space Studies, New York, New York, USA.

[3] Also at Department of Earth and Ocean Sciences, University of British Columbia, Vancouver, British Columbia, Canada.

[4] Also at Physics Department, Langara College, Vancouver, British Columbia, Canada.

[5] Department of Earth System Science, University of California, Irvine, California, USA.

Copyright 2008 by the American Geophysical Union.
0148-0227/08/2006JC003976$09.00

Ω_f path, η is also the density of $\Omega_i \rightarrow \Omega_f$ paths per unit volume and residence time. *Holzer and Primeau* [2006] have recently used the path density η to trace out the interbasin deep branch of the ocean circulation in a steady state global model, which showed that advection along the oceans' major current systems accounts for less than half of the surface-to-surface transport.

[5] The goals of this paper are to fully develop the path-density diagnostic and its relationship to ventilation-rate distributions. The later were recently argued to be necessary to properly characterize water mass ventilation rates [*Primeau and Holzer*, 2006; *Hall et al.*, 2007]. The character of the path density, including its long-residence-time asymptotic structure, will be illustrated using a global general circulation model. We will argue that the qualitative character of the oceanic surface-to-surface transport revealed by our diagnostics is likely to be shared by the real ocean. The picture of ocean transport that emerges sheds new light on the structure of both modeled and observed long-lived tracer distributions. Depleted radiocarbon in the deep N Pacific is shown to be consistent with the deep N Pacific being a stagnant "holding pen" that should not be interpreted as a conveyor terminus.

2. Tracking Water From and to the Surface

[6] We track water since its last contact with a surface patch, Ω_i, by using the boundary-propagator $\mathcal{G}$ [e.g., *Holzer and Hall*, 2000; *Primeau*, 2005]. The boundary propagator is a type of Green function, which is defined so that $\mathcal{G}(\mathbf{r}, t|\Omega_i, t_i)\, dt_i$ is the mass fraction of water at $(\mathbf{r}, t)$ that had last contact with surface patch Ω_i during the time interval $(t_i, t_i + dt_i)$. The boundary propagator, $\mathcal{G}$, also called the transit-time distribution (TTD) [*Haine and Hall*, 2002], labels fluid elements as they are ventilated into the ocean on Ω_i at time t_i. The equation of motion for $\mathcal{G}$ is

$$\frac{\partial}{\partial t}[\rho\mathcal{G}(\mathbf{r}, t|\Omega_i, t_i)] + \nabla \cdot \mathbf{J}(\mathbf{r}, t|\Omega_i, t_i) = 0, \tag{1}$$

subject to the surface boundary condition

$$\mathcal{G}(\mathbf{r}, t|\Omega_i, t_i) = \begin{cases} \delta(t - t_i) & \text{if } \mathbf{r} \in \Omega_i \\ 0 & \text{otherwise,} \end{cases} \tag{2}$$

where

$$\mathbf{J}(\mathbf{r}, t|\Omega_i, t_i) \equiv [\rho\mathbf{u} - \rho\mathbf{K}\nabla]\mathcal{G}(\mathbf{r}, t|\Omega_i, t_i) \tag{3}$$

is the mass flux of $\mathcal{G}$ for fluid density ρ, velocity $\mathbf{u}$, and eddy-diffusivity tensor $\mathbf{K}$. The diffusivity $\mathbf{K}$ is a function of position and time (although for illustration we will only use a steady model), and contains both diapycnal and isopycnal components, the latter being isotropic in our model. While $\mathbf{K}$ would be diagonal in a local coordinate system aligned with the isopycnal surfaces, in our model $\mathbf{K}$ is represented in Cartesian latitude-longitude-depth coordinates and hence contains diagonal and off-diagonal components. At boundaries other than the surface, $\mathbf{J} \cdot \widehat{n} = 0$, where $\widehat{n}$ is a unit vector normal to the boundary.

[7] Analogously, we compute $\widetilde{\mathcal{G}}(\mathbf{r}, t|\Omega_f, t_f)dt_f$, the mass fraction of water at $(\mathbf{r}, t)$ that will make its first surface contact with patch Ω_f in the time interval $(t_f, t_f + dt_f)$. Physically, $\widetilde{\mathcal{G}}(\mathbf{r}, t|\Omega_f, t_f)$ is given by the flux of water onto Ω_f that was labeled at $(\mathbf{r}, t)$. We compute $\widetilde{\mathcal{G}}$ efficiently for every point $(\mathbf{r}, t)$ in the ocean by exploiting the fact that $\widetilde{\mathcal{G}}(\mathbf{r}, t|\Omega_f, t_f)$ is governed by the time-reversed adjoint of equation (1) [*Holzer and Hall*, 2000]. Conceptually, we repeat our calculations for $\mathcal{G}$ with a time-reversed flow so that last contact becomes first contact in the time-forward flow. However, diffusion in this time-reversed flow must still act to disperse tracer, as reflected by the fact that $\widetilde{\mathcal{G}}$ evolves with the time-reversed adjoint flow, that is, the flow governed by the mathematical adjoint of the transport operator, which is integrated backward in time. The equation of motion for $\widetilde{\mathcal{G}}$ therefore parallels (1), with the delta function $\delta(t - t_f)$ applied on Ω_f, and with $\mathbf{J}$ replaced with $\widetilde{\mathbf{J}}(\mathbf{r}, t|\Omega_f, t_f) \equiv [-\rho\mathbf{u} - \rho\mathbf{K}^T\nabla]\widetilde{\mathcal{G}}(\mathbf{r}, t|\Omega_f, t_f)$, where $\nabla \cdot \rho\mathbf{u} = 0$ is assumed, and $\mathbf{K}^T$ denotes the transpose of $\mathbf{K}$. Thus $\widetilde{\mathcal{G}}(\mathbf{r}, t|\Omega_f, t_f)$ is a propagator for the time-reversed adjoint flow, which labels fluid elements as they become exposed to the atmosphere (that is, enter the time-reversed adjoint flow) at time t_f on surface patch Ω_f.

2.1. Path Density, η

[8] The path density bins the ocean's fluid elements according to how long their surface-to-surface journey takes, according to where they enter and exit the ocean interior, and according to the interior location $\mathbf{r}$ where they reside at time t. More precisely, the path density $\eta(\mathbf{r}, \tau, \Omega_i, \Omega_f; t)$ is defined so that $\eta(\mathbf{r}, \tau, \Omega_i, \Omega_f; t)d^3r d\tau$ is the mass fraction in volume element d^3r at point $(\mathbf{r}, t)$ that will make the $\Omega_i \rightarrow \Omega_j$ journey in time $\tau \in (\tau, \tau + d\tau)$. Since each fluid element comprising this mass fraction traces out a path from Ω_i to Ω_f, $\eta(\mathbf{r}, \tau, \Omega_i, \Omega_f; t)$ is also the density of $\Omega_i \rightarrow \Omega_f$ paths. The path density η is a density per unit volume and per unit residence time, the density in residence time being crucial here because it allows us to calculate transport rates. We will now give a heuristic construction of η – for a more rigorous derivation, see Appendix A.

[9] The mass fraction of a water parcel at point $(\mathbf{r}, t)$ that had last Ω_i contact during $(t_i, t_i + dt_i)$ is given by $\mathcal{G}(\mathbf{r}, t|\Omega_i, t_i)dt_i$, while the mass fraction of the same parcel that will make first contact with Ω_f during $(t_f, t_f + dt_f)$ is given by $\widetilde{\mathcal{G}}(\mathbf{r}, t|\Omega_f, t_f)dt_f$ (see Figure 1). The product of these fractions is the mass faction of water at $(\mathbf{r}, t)$ that makes the $\Omega_i \rightarrow \Omega_f$ journey starting during $(t_i, t_i + dt_i)$ and ending during $(t_f, t_f + dt_f)$. To obtain the density per unit volume, this mass fraction must be multiplied by the fluid density, which we divide by the mass of the ocean, M, for convenient normalization [see equation (5) for the precise normalization with respect to all the distributed variables of η]. Finally, integrating over all possible values of initial times $t_i \leq t$ and final times $t_f \geq t$ that are separated by the residence time τ (that is, integrating subject to the constraint that $t_f - t_i = \tau$) gives the mass fraction of water at $(\mathbf{r}, t)$ that makes the $\Omega_i \rightarrow \Omega_f$ trip in a time $\tau \in (\tau, \tau + d\tau)$. Using these arguments, or from the derivation of Appendix A, we obtain

$$\eta(\mathbf{r}, \tau, \Omega_i, \Omega_f; t) = \frac{\rho(\mathbf{r}, t)}{M} \int_{t-\tau}^{t} dt_i\, \widetilde{\mathcal{G}}(\mathbf{r}, t|\Omega_f, t_i + \tau)\, \mathcal{G}(\mathbf{r}, t|\Omega_i, t_i). \tag{4}$$

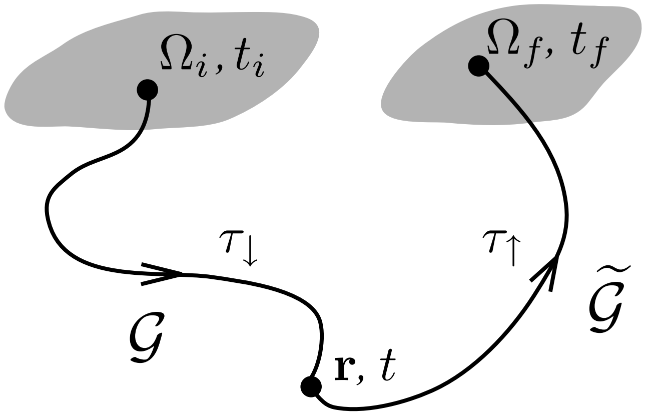

Figure 1. To construct the density, per unit volume and per unit residence time, of paths at point ($\mathbf{r}$, t) connecting patch Ω_i to patch Ω_f, one needs to know the boundary propagators $\mathcal{G}$ and $\widetilde{\mathcal{G}}$. The quantity $\mathcal{G}(\mathbf{r}, t|\Omega_i, t_i)dt_i$ gives the mass fraction of water at ($\mathbf{r}$, t) that had last surface contact during time interval (t_i, $t_i + dt_i$) with Ω_i, while $\widetilde{\mathcal{G}}(\mathbf{r}, t|\Omega_f, t_f)dt_f$ gives the mass fraction of water at ($\mathbf{r}$, t) that will make first surface contact during time interval (t_f, $t_f + dt_f$) with Ω_f. The path density, η, for residence time interval (τ, $\tau + d\tau$) is calculated by multiplying these fractions and integrating over all t_i and t_f subject to the constraint $t_i - t_f = \tau$. At ($\mathbf{r}$, t), the transit time since last contact with Ω_i is $\tau_\downarrow = t - t_i$, and the transit time to first contact with Ω_f is $\tau_\uparrow = t_f - t$. The constraint $t_i - t_f = \tau$ is equivalent to $\tau_\downarrow + \tau_\uparrow = \tau$.

As constructed in Appendix A, using the fact that $\mathcal{G}$, $\widetilde{\mathcal{G}}$, and ρ/M are normalized distributions, the density η is guaranteed to be a normalized distribution, that is,

$$\sum_{\Omega_i}\sum_{\Omega_f}\int_0^\infty d\tau \int_V d^3\mathbf{r}\ \eta(\mathbf{r}, \tau, \Omega_i, \Omega_f; t) = 1, \qquad (5)$$

where the spatial integral is over the entire ocean volume, V.

[10] The temporal moments $\int_0^\infty d\tau\tau^n\eta$ can be expressed straightforwardly in terms of the moments of the transit-time distributions $\mathcal{G}$ and $\widetilde{\mathcal{G}}$, as shown in Appendix B. We will be particularly interested in the residence-time integrated path density, $\int_0^\infty d\tau\eta$, which can be obtained efficiently as the product of the water mass fractions $f(\mathbf{r}, t|\Omega_i) \equiv \int_0^\infty d\tau_\downarrow \mathcal{G}(\mathbf{r}, t|\Omega_i, t - \tau_\downarrow)$ and $\widetilde{f}(\mathbf{r}, t|\Omega_f) \equiv \int_0^\infty d\tau_\uparrow \widetilde{\mathcal{G}}(\mathbf{r}, t|\Omega_f, t + \tau_\uparrow)$. Physically, $f(\mathbf{r}, t|\Omega_i)$ is the mass fraction of water at ($\mathbf{r}$, t) that had last contact with the surface on Ω_i, regardless of the $\Omega_i \rightarrow \mathbf{r}$ transit time $\tau_\downarrow$. Similarly, $\widetilde{f}(\mathbf{r}, t|\Omega_f)$ is the mass fraction of water at point ($\mathbf{r}$, t) that will make its first surface contact on Ω_f, regardless of the $\mathbf{r} \rightarrow \Omega_f$ transit time $\tau_\uparrow$. For our steady ocean model, the water mass fractions f and $\widetilde{f}$, as well as the higher-order moments of $\mathcal{G}$ or $\widetilde{\mathcal{G}}$, are time independent and can easily be obtained without first time stepping the equations of motion of $\mathcal{G}$ and $\widetilde{\mathcal{G}}$. Instead, one can directly invert moments of the equation of motion organized in matrix form [e.g., *Primeau*, 2005].

2.2. Transport-Volume and Flux Distributions

[11] The transport-volume distribution, $\mathcal{R}$, is defined so that $\mathcal{R}(\tau, \Omega_i, \Omega_f; t)d\tau$ is the volume fraction of the ocean at time t whose residence time, from entry on Ω_i to exit on Ω_f, lies in the interval $\tau \in (\tau, \tau + d\tau)$. The distribution $\mathcal{R}$ is readily obtained by integrating the local volume fraction of Ω_i-to-Ω_f water per unit residence time, $\eta(\mathbf{r}, \tau, \Omega_i, \Omega_f; t)d^3r$, over the entire ocean:

$$\mathcal{R}(\tau, \Omega_i, \Omega_f; t) = \int_V d^3r\ \eta(\mathbf{r}, \tau, \Omega_i, \Omega_f; t). \qquad (6)$$

Because $\mathcal{R}(\tau, \Omega_i, \Omega_f; t)$ can also be thought of as the joint pdf of continuous residence time and discrete entry and exit location, *Primeau and Holzer* [2006] referred to $\mathcal{R}$ as the residence-time pdf.

[12] The distribution $\mathcal{R}$ is intimately related to the flux of water making the $\Omega_i \rightarrow \Omega_f$ journey. As shown in Appendix C, one can derive that

$$\mathcal{R}(\tau, \Omega_i, \Omega_f; t) = \frac{1}{M}\int_{t-\tau}^{t} dt_i \phi_\downarrow(\Omega_i, t_i; \Omega_f, \tau), \qquad (7)$$

or equivalently

$$\mathcal{R}(\tau, \Omega_i, \Omega_f; t) = \frac{1}{M}\int_{t}^{t+\tau} dt_f \phi_\uparrow(\Omega_f, t_f; \Omega_i, \tau), \qquad (8)$$

where $\phi_\downarrow(\Omega_i, t_i; \Omega_f, \tau) \equiv \int_{\Omega_f} d\mathbf{a} \cdot \mathbf{J}(\mathbf{r}, t_i + \tau|\Omega_i, t_i)$, or equivalently $\phi_\downarrow(\Omega_i, t_i; \Omega_f, \tau) \equiv \int_{\Omega_i} d\mathbf{a} \cdot \widetilde{\mathbf{J}}(\mathbf{r}, t_i|\Omega_f, t_i + \tau)$. Physically, $\phi_\downarrow(\Omega_i, t_i; \Omega_f, \tau)d\tau$ is the rate at which water with a residence time $\tau \in (\tau, \tau + d\tau)$ enters through Ω_i. Similarly $\phi_\uparrow(\Omega_f, t_f; \Omega_i, \tau)d\tau$ is the rate at which water with a residence time $\tau \in (\tau, \tau + d\tau)$ is re-exposed to the atmosphere on Ω_f. We refer to $\phi_\downarrow$ and $\phi_\uparrow$ as flux-density distributions. The properties of $\phi_\downarrow$ and $\phi_\uparrow$ were discussed in detail by *Primeau and Holzer* [2006] in the context of water mass ventilation.

[13] Physically, (7) and (8) express the fact that the mass of water in the ocean with residence time $\tau \in (\tau, \tau + d\tau)$, that is $M\mathcal{R}d\tau$, can be obtained by accumulating for a time τ the flux of water with residence time in the interval (τ, $\tau + d\tau$) that enters the interior through Ω_i in the case of (7), or that exits the interior through Ω_f in the case of (8). In other words, the flux of water with $\tau \in (\tau, \tau + d\tau)$ acting for a time τ will "flush out" precisely the volume in residence-time interval (τ, $\tau + d\tau$) that was in the ocean when the flushing started.

2.3. Simplifications for the Steady State

[14] Although our development is general, we will illustrate the character of the oceanic surface-to-surface path density using a steady state circulation model. It is therefore useful to briefly discuss the convenient simplifications that occur for steady flow.

[15] Steady flow allows us to use less complex notation and eliminates the parametric dependence of $\mathcal{R}$ and η on time, t. With the notation $\mathcal{G}(\mathbf{r}, \tau_\downarrow|\Omega) \equiv \mathcal{G}(\mathbf{r}, t + \tau_\downarrow|\Omega, t)$ and for $\rho = M/V$ constant, we then have

$$\eta(\mathbf{r}, \tau, \Omega_i, \Omega_f) = \frac{1}{V}\int_0^\tau d\tau_\downarrow\ \widetilde{\mathcal{G}}(\mathbf{r}, \tau - \tau_\downarrow|\Omega_f)\mathcal{G}(\mathbf{r}, \tau_\downarrow|\Omega_i). \qquad (9)$$

In steady state $\phi_\downarrow$ and $\phi_\uparrow$ are independent of t_i or t_f and we define $\phi_\downarrow(\Omega_i, t_i; \Omega_f, \tau) = \phi_\uparrow(\Omega_f, t_f; \Omega_i, \tau) \equiv \phi(\tau, \Omega_i, \Omega_f)$. The

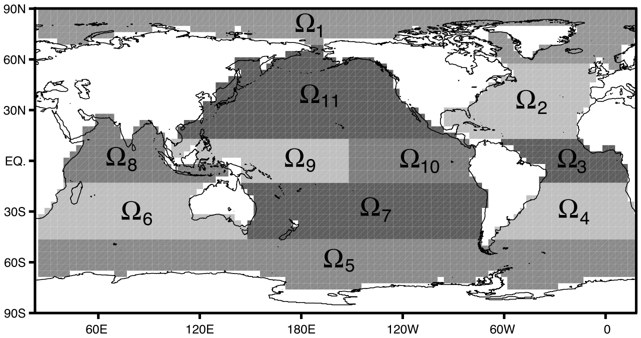

Figure 2. Map defining the eleven surface patches used. The union of all eleven patches covers the entire model ocean surface. The areas of the eleven patches have the values: A_1 = 1.72, A_2 = 3.02, A_3 = 1.67, A_4 = 2.41, A_5 = 5.12, A_6 = 3.39, A_7 = 4.81, A_8 = 2.74, A_9 = 2.61, A_{10} = 2.32, and A_{11} = 5.79, in units of 10^{13} m^2.

time integrals of (7) and (8) then reduce to multiplication by τ so that the flux-density distribution is given by

$$\phi(\tau, \Omega_i, \Omega_f) = \frac{M\mathcal{R}(\tau, \Omega_i, \Omega_f)}{\tau}. \qquad (10)$$

[16] The total volume of fluid elements that at any moment is making its way from Ω_i to Ω_f, regardless of residence time, is given by

$$\mathcal{V}(\Omega_i, \Omega_f) = V \int_0^\infty d\tau \mathcal{R}(\tau, \Omega_i, \Omega_f), \qquad (11)$$

while the total mass flux of water that enters the interior through Ω_i and is destined to be re-exposed to the atmosphere on Ω_f, regardless of residence time, is given by

$$\Phi(\Omega_i, \Omega_f) = \int_0^\infty d\tau \phi(\tau, \Omega_i, \Omega_f). \qquad (12)$$

Care must be taken when calculating the flux $\Phi(\Omega_i, \Omega_f)$. If Ω_i and Ω_f overlap (or even share edges), $\phi(\tau, \Omega_i, \Omega_f)$ has a non-integrable singularity at $\tau = 0$ [*Primeau and Holzer*, 2006] (for the case of $\Omega_i = \Omega_f$ being the entire surface, this was also shown by *Hall and Holzer* [2003]). The total $\Omega_i \rightarrow \Omega_f$ transport volume $\mathcal{V}(\Omega_i, \Omega_f)$, on the other hand, is always well defined and finite regardless of the choices for Ω_i and Ω_f, because the total volume of the ocean is finite.

3. Illustrations From a Steady State Global Model

[17] To illustrate the utility of the path-density diagnostic in revealing advective-diffusive oceanic transport pathways and their associated transport volume and flux distributions, we calculate η for the surface patches defined in Figure 2 using the steady state global ocean model of *Primeau* [2005]. This off-line model is based on the time-averaged velocity and eddy-diffusivity tensor fields from dynamical simulations with a full OGCM that uses the KPP [*Large et al.*, 1994] and GM [*Gent and McWilliams*, 1990] mixing schemes. The background dia- and isopycnal diffusivities are 0.5×10^{-5} and 1000 m^2/s. The OGCM used is a version of the ocean component of the climate model of the Canadian Centre for Climate Modelling and Analysis, itself based on version 1.3 of the NCAR CSM Ocean Model [*Pacanowski et al.*, 1993]. For details of the OGCM run on which the off-line model is based, see *Primeau* [2005].

[18] The off-line model (like its parent OGCM) uses second-order centered differences on a grid with 29 levels in the vertical ranging in thickness from 50 m near the surface to 300 m near the bottom, and a $\sim 3.75° \times 3.75°$ horizontal resolution. Time-evolving boundary propagators were computed by exponentiating the steady state transport operator over finite time steps using the Expokit software [*Sidje*, 1998]. Moments of pdfs were computed by direct matrix inversion of their steady state equations using the multifrontal approach of the MUMPS solver [*Amestoy et al.*, 2001]. Eigenfunctions of the forward and adjoint transport operator were computed using the implicitly restarted Arnoldi method [*Lehoucq et al.*, 1998] as implemented in MATLAB's sparse matrix package.

3.1. Dependence of Path Density on Residence Time

[19] Figures 3–8 show the densities of paths connecting the deep-water formation regions of the high-latitude oceans with their key re-exposure regions. The spatial patterns of the path densities are summarized in terms of their depth integrals and their zonal averages for each basin. We show the patterns at fixed values of the residence time, τ. For the $\Omega_1 \rightarrow \Omega_{10}$ and $\Omega_5 \rightarrow \Omega_5$ cases, the τ-integrated path densities are also shown.

[20] The spatial structure of the path-density for non-overlapping patches is determined by where τ falls with respect to the mode, τ_ϕ, of the corresponding flux-density distribution, ϕ. [The mode of the distribution, $\phi(\tau)$, is the value of τ for which ϕ attains its maximum value.] The flux-density distribution $\phi(\tau)$, together with its cumulative distribution $\int_0^\tau d\tau' \phi(\tau')$ and the corresponding transport-volume distributions, $\mathcal{R}(\tau)$ and $\int_0^\tau d\tau' \mathcal{R}(\tau')$, are also shown on Figures 3–8. For non-overlapping patches, $\phi(\tau)$ is non-singular at $\tau = 0$, and we show η for $\tau^-_{\phi/2}$, τ_ϕ, $\tau^+_{\phi/2}$, and for τ = 3000 a, where $\tau^-_{\phi/2}$ and $\tau^+_{\phi/2}$ are the residence times below and above τ_ϕ, for which $\phi(\tau)$ attains half its peak value [that is, $\phi(\tau^-_{\phi/2}) = \phi(\tau^+_{\phi/2}) = \phi(\tau_\phi)/2$]. For the case of

Figure 3. The $\Omega_1 \rightarrow \Omega_{10}$ path density (N Atlantic to tropical eastern Pacific) vertically integrated, and zonally averaged for each basin at the residence times, τ, indicated and also integrated over all τ. For each τ, and the τ-integrated case, the vertical integrals have been normalized by their maximum value, $\max_v$, and the zonal averages have been normalized by their maximum value (over all three basins), $\max_z$. For the case of a specified τ, the units of $\max_v$ are m^{-2} a^{-1}, and the units of $\max_z$ are m^{-3} a^{-1}. For the τ-integrated case, the units of $\max_v$ are m^{-2}, and the units of $\max_z$ are m^{-3}. The contour interval is 0.125. The Ω_1 and Ω_{10} patches are outlined by heavy black lines. The curves in the rightmost plots show the associated flux density (solid) and transport-volume density (dashed) normalized by their peak value, as well as their cumulative distributions. The values of τ considered are indicated by grey vertical lines. See color plates if viewing the print version.

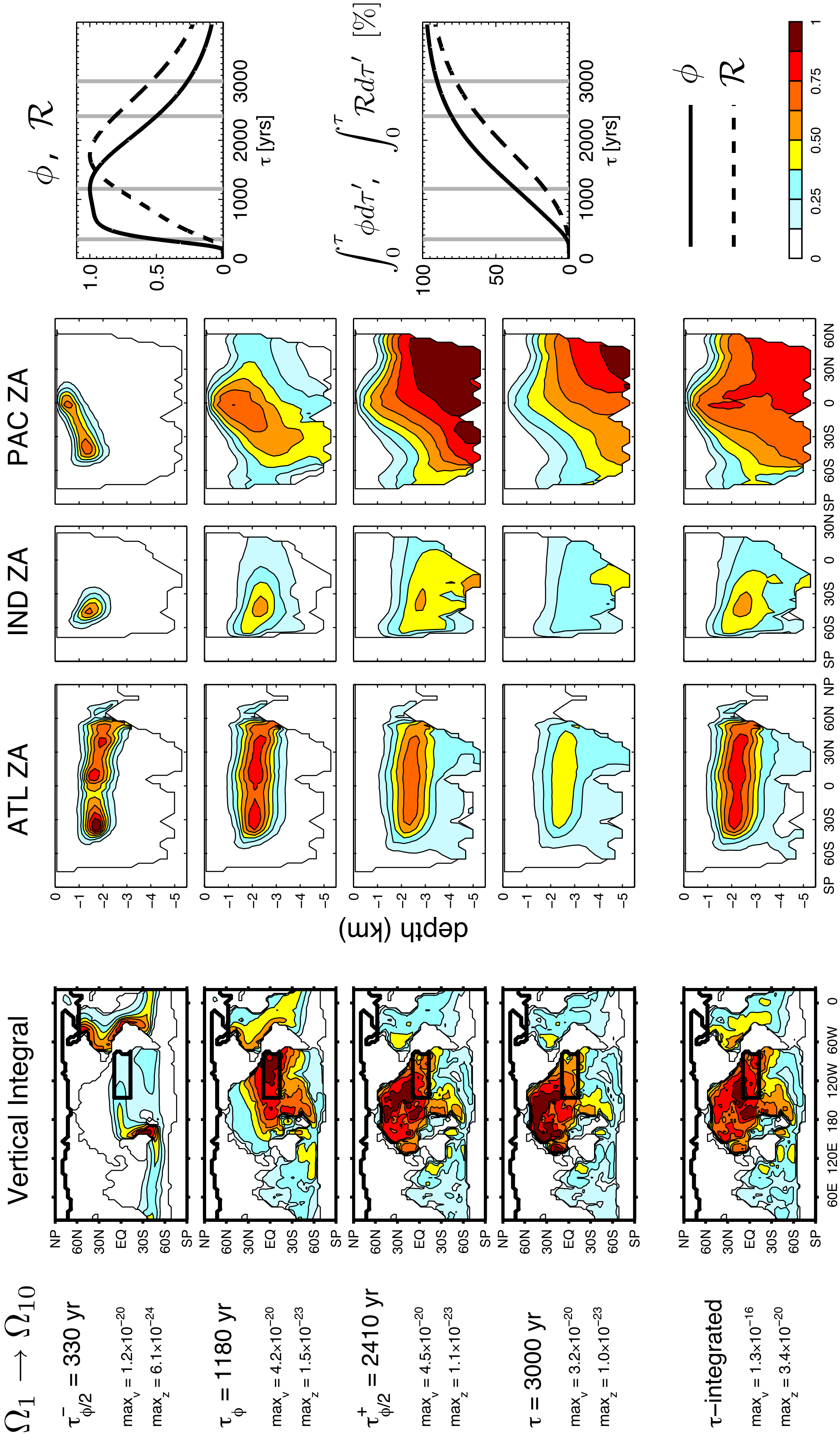

$\Omega_1 \longrightarrow \Omega_{10}$
$\tau^-_{\phi/2}$ = 330 yr
max$_v$ = 1.2×10^{-20}
max$_z$ = 6.1×10^{-24}
τ_ϕ = 1180 yr
max$_v$ = 4.2×10^{-20}
max$_z$ = 1.5×10^{-23}
$\tau^+_{\phi/2}$ = 2410 yr
max$_v$ = 4.5×10^{-20}
max$_z$ = 1.1×10^{-23}
τ = 3000 yr
max$_v$ = 3.2×10^{-20}
max$_z$ = 1.0×10^{-23}
τ–integrated
max$_v$ = 1.3×10^{-16}
max$_z$ = 3.4×10^{-20}
Vertical Integral
ATL ZA
IND ZA
PAC ZA
NP 60N 30N EQ 30S 60S SP
60E 120E 180 120W 60W 0
depth (km)
0 −1 −2 −3 −4 −5
SP 60S 30S 0 30N 60N NP
SP 60S 30S 0 30N
SP 60S 30S 0 30N 60N
ϕ, $\mathcal{R}$
1.0 0.5 0
0 1000 2000 3000
τ [yrs]
$\int_0^\tau \phi d\tau'$, $\int_0^\tau \mathcal{R} d\tau'$ [%]
100 50 0
ϕ
$\mathcal{R}$
0 0.25 0.50 0.75 1

Figure 3

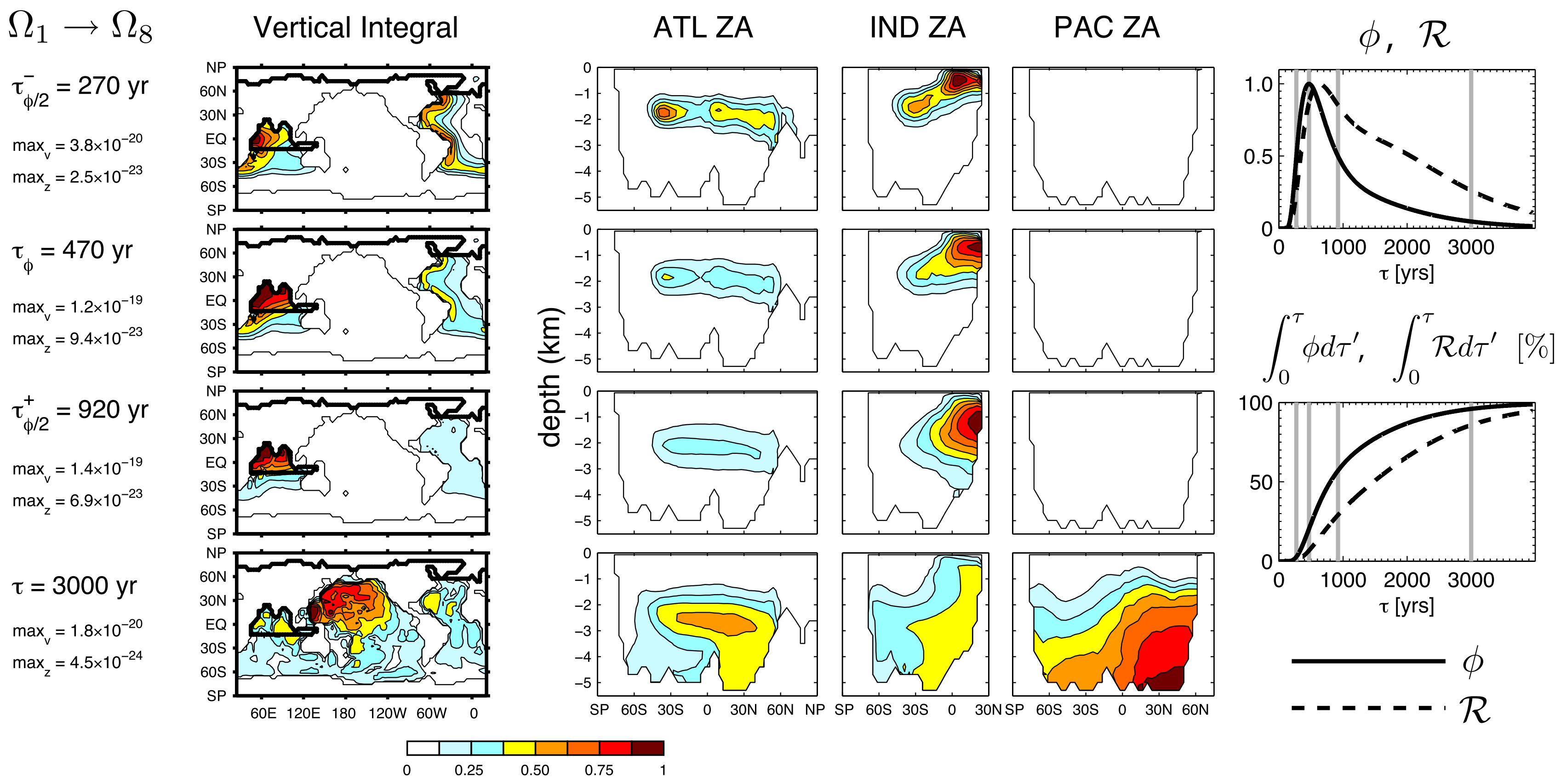

Figure 4. As Figure 3 for the $\Omega_1 \rightarrow \Omega_8$ path density (N Atlantic to tropical Indian Ocean), without the residence-time integrated path density. See color plates if viewing the print version.

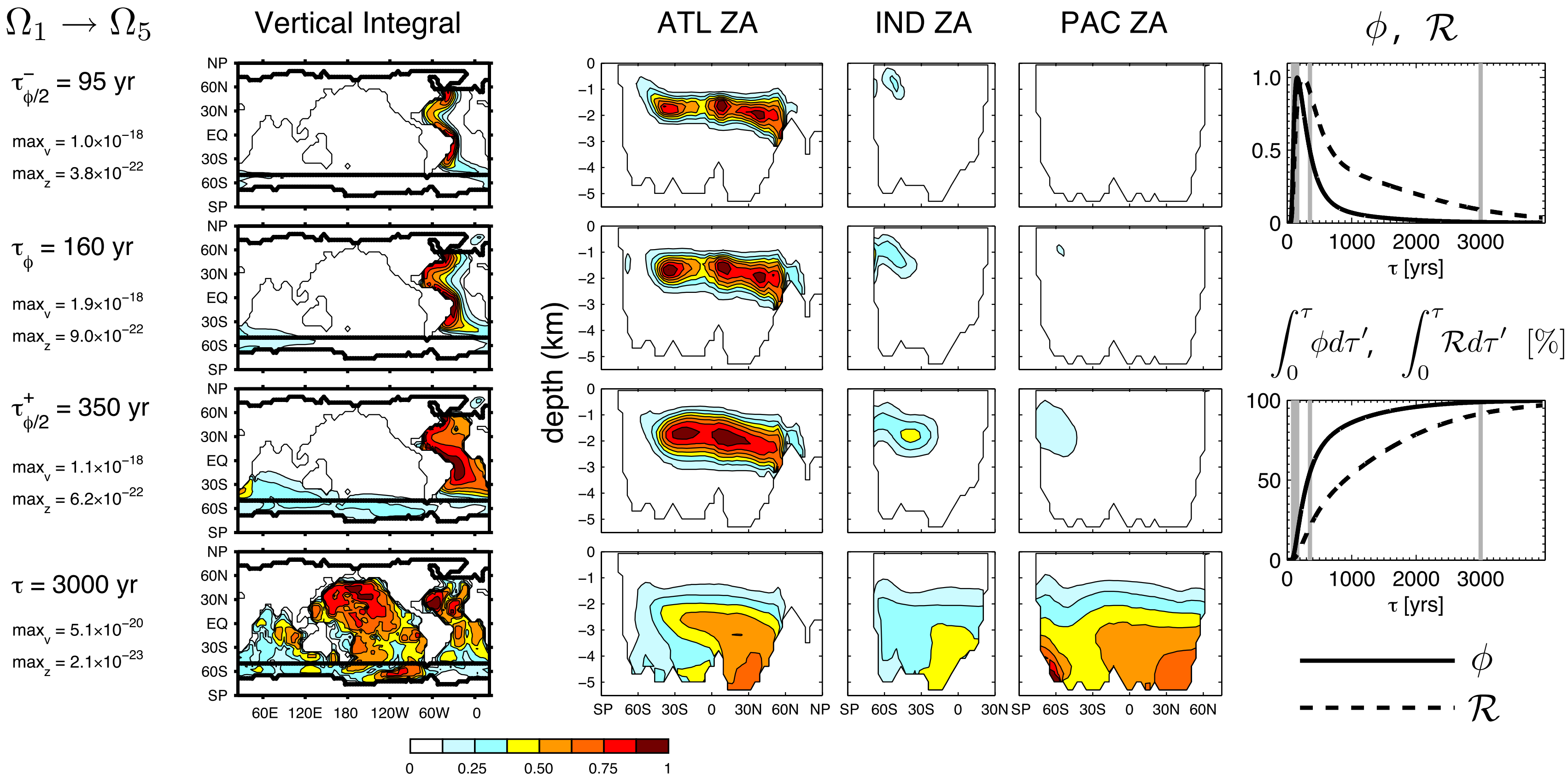

Figure 5. As Figure 4 for the $\Omega_1 \rightarrow \Omega_5$ path density (North Atlantic to Southern Ocean). See color plates if viewing the print version.

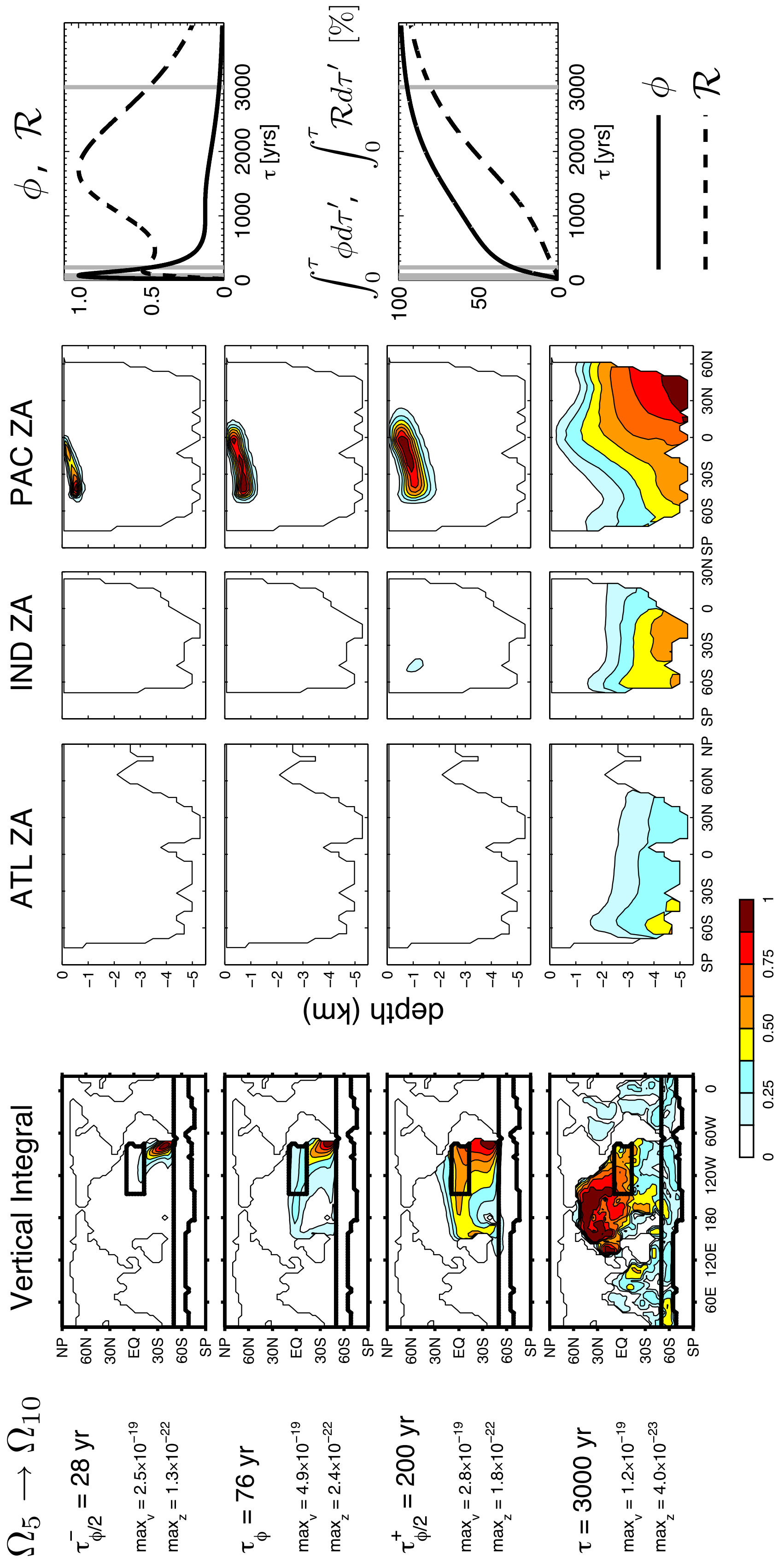

Figure 6. As Figure 4 for the $\Omega_5 \rightarrow \Omega_{10}$ path density (Southern Ocean to tropical eastern Pacific). See color plates if viewing the print version.

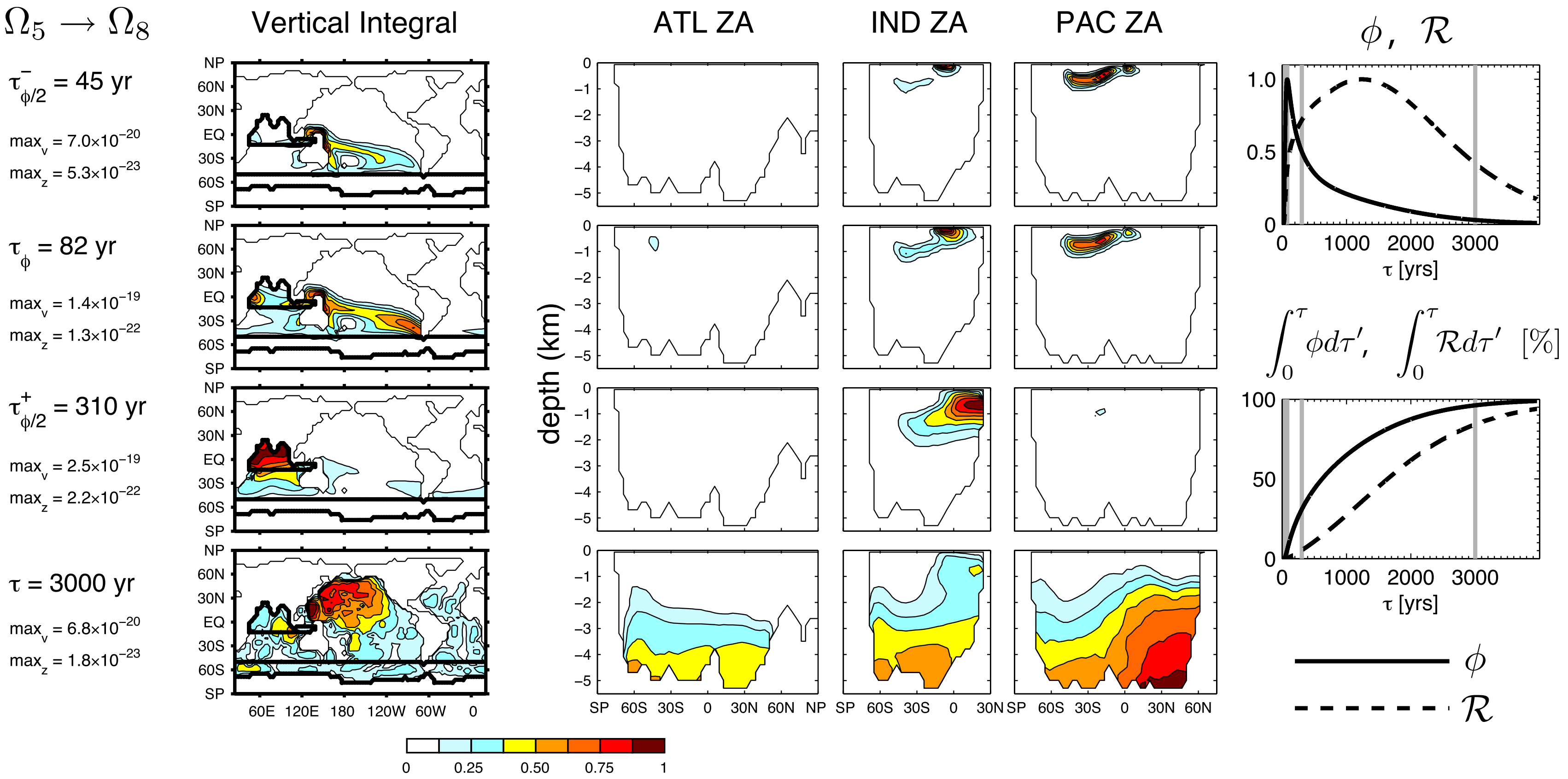

Figure 7. As Figure 4 for the $\Omega_5 \rightarrow \Omega_8$ path density (Southern Ocean to tropical Indian Ocean). See color plates if viewing the print version.

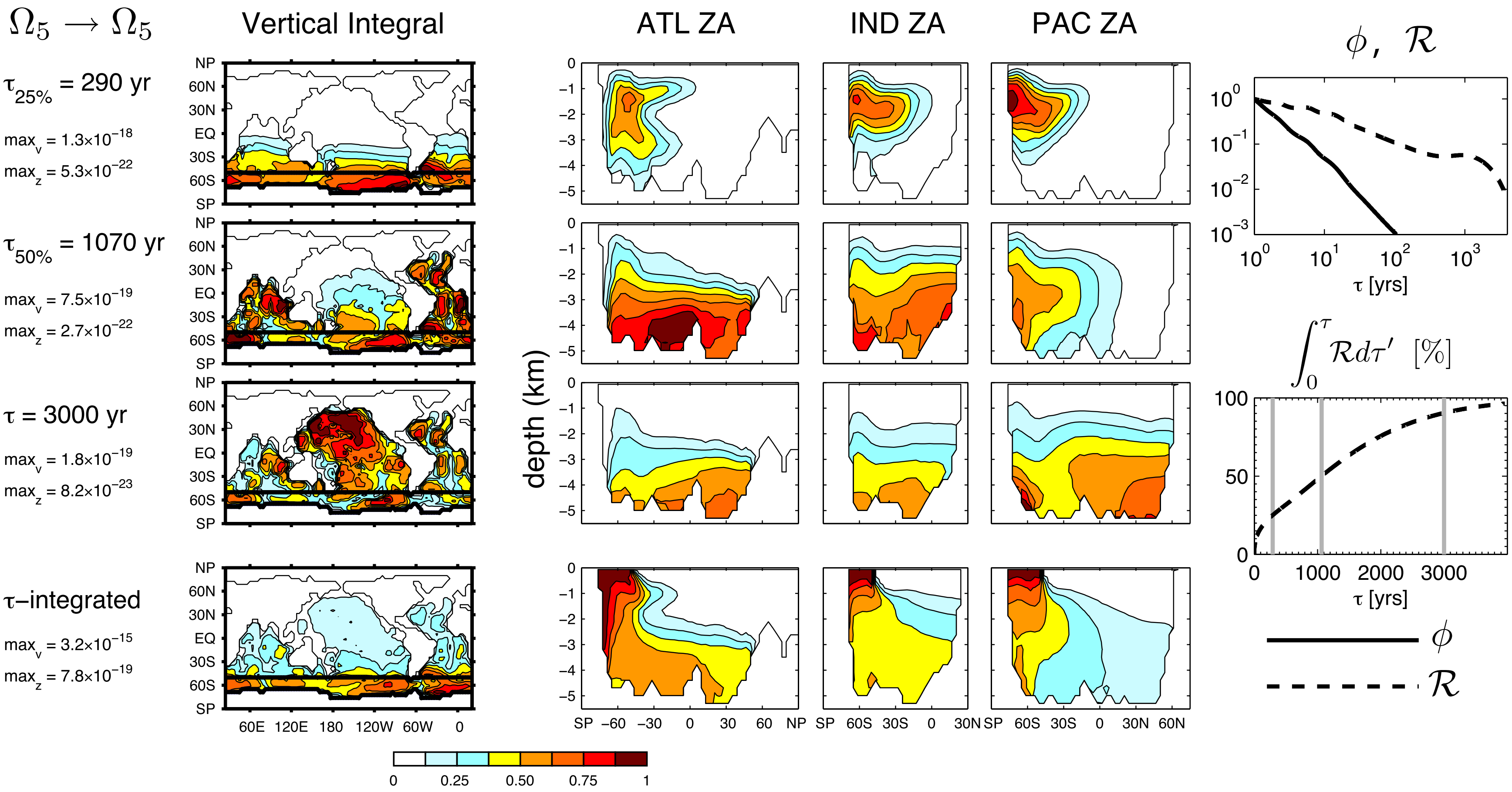

Figure 8. As Figure 3 for the $\Omega_5 \rightarrow \Omega_5$ path density (Southern Ocean to Southern Ocean). The residence times $\tau_{25\%}$ = 290 a and $\tau_{50\%}$ = 1070 a correspond to the 25% and 50% quantiles of $\mathcal{R}(\tau, \Omega_5, \Omega_5)$. Because $\phi(\tau, \Omega_5, \Omega_5)$ and $\mathcal{R}(\tau, \Omega_5, \Omega_5)$ are singular at $\tau = 0$ and rapidly decreasing, we show log-log plots of $\phi(\tau, \Omega_5, \Omega_5)/\phi(1\text{ a}, \Omega_5, \Omega_5)$ and $\mathcal{R}(\tau, \Omega_5, \Omega_5)/\mathcal{R}(1\text{ a}, \Omega_5, \Omega_5)$. Because the singularity of $\phi(\tau, \Omega_5, \Omega_5)$ gives a non-integrable cumulative flux distribution, we show only the cumulative transport-volume distribution $\int_0^\tau \mathcal{R}(\tau', \Omega_5, \Omega_5) d\tau'$. See color plates if viewing the print version.

waters that are both ventilated and re-exposed on the same patch (Figure 8 for $\Omega_5 \rightarrow \Omega_5$ transport), the corresponding $\phi(\tau)$ has a non-integrable singularity at $\tau = 0$ [*Primeau and Holzer*, 2006], so that $\tau_\phi = 0$. In this case, we therefore show η for the residence times $\tau_{25\%}$ and $\tau_{50\%}$ corresponding to the 25% and 50% quantiles of $\mathcal{R}$. (The physical meaning of the X% quantile of $\mathcal{R}$ is that water with residence times less than $\tau_{X\%}$ constitutes X% of the volume fraction of the ocean in transit from Ω_i to Ω_f.)

3.1.1. Path Density of Waters Formed on the North Atlantic Surface

[21] The deep water formed on Ω_1 is re-exposed to the atmosphere primarily in the Southern Ocean through upwelling and mixing, and in the tropical eastern Pacific, tropical Indian Ocean, and tropical eastern Atlantic through upwelling caused by divergent Ekman transport. (Although Ω_1 includes the entire Arctic, deepwater is formed predominantly in its N-Atlantic portion.) Detailed maps of the local re-exposure flux of Ω_1 waters can be found in the work by *Primeau and Holzer* [2006]. To emphasize interbasin transport, we focus here on paths from Ω_1 to Ω_{10} (tropical eastern Pacific), Ω_8 (tropical Indian Ocean), and Ω_5 (Southern Ocean). The total fluxes connecting these patch pairs are [*Primeau and Holzer*, 2006] $\Phi(\Omega_1, \Omega_{10}) = 0.43$ Sv, $\Phi(\Omega_1, \Omega_8) = 0.48$ Sv, and $\Phi(\Omega_1, \Omega_5) = 6.5$ Sv. The total flux from Ω_1 to the entire Pacific, excluding Ω_5, is 1.2 Sv, and the total flux from Ω_1 to the Indian Ocean (the union of Ω_6 and Ω_8) is 1.1 Sv. The corresponding total transport volume fractions are $\mathcal{V}(\Omega_1, \Omega_{10})/V = 1.7\%$, $\mathcal{V}(\Omega_1, \Omega_8)/V = 1.3\%$, and $\mathcal{V}(\Omega_1, \Omega_5)/V = 8.8\%$.

[22] Figure 3 shows the $\Omega_1 \rightarrow \Omega_{10}$ path density. The plots for $\tau^{-}_{\phi}/2 = 330$ a show the structure of the fast paths connecting the N Atlantic to the tropical eastern Pacific via the classical routes of Broecker's great ocean conveyor (GOC, [*Broecker*, 1991]). The fast paths follow the ocean's major current systems as seen in the 330-a vertical integral: The Atlantic deep western boundary current, followed by the Antarctic Circumpolar Current, the western boundary currents past Australia and New Zealand to shallower equatorial depths (see the Pacific zonal average), where the Equatorial Undercurrent delivers the water to Ω_{10}. The 330-a zonal averages show that these fast routes lie primarily between 1 and 2 km depth, coinciding in the Atlantic with the model's N-Atlantic deep water. In the Pacific zonal average the ascent to the Equatorial Undercurrent is evident. As the cumulative distributions show (see the curves of $\int_0^\tau \phi d\tau'$ and $\int_0^\tau \mathcal{R} d\tau'$ versus τ), waters with residence times of $\tau^{-}_{\phi/2}$ (indicated by the first vertical grey line) or less, constitute very little of the $\Omega_1 \rightarrow \Omega_{10}$ flux and transport volume (1.6% and 0.28%, respectively).

[23] At the mode $\tau_\phi = 1180$ a of the $\Omega_1 \rightarrow \Omega_{10}$ flux-density distribution, the path density is seen to be concentrated under the Ω_{10} out patch in the 1180-a vertical integral and Pacific zonal average of Figure 3. This is a consequence of the zero-concentration surface boundary condition which causes the flux into the model's top layer to be primarily diffusive, and hence proportional to the concentration gradient, so that the maximum flux onto the Ω_{10} surface patch occurs when the concentration of Ω_1-to-Ω_{10} waters just under Ω_{10} reaches its maximum value. Because the model flow is steady, the maximum flux into the N-Atlantic entering from patch Ω_1 also occurs at $\tau = \tau_\phi$. However, in contrast to the re-exposure flux, the flux entering from Ω_1 is maintained through highly localized deep convection (parameterized as enhanced diffusion over many layers), and therefore does not correspond to a concentration of Ω_1-to-Ω_{10} waters under Ω_1. Because of the long tail of $\phi(\tau, \Omega_1, \Omega_{10})$ to the right of its peak seen in the ϕ versus τ curve, waters with residence times $\tau \leq \tau_\phi$ constitute less than half (36%) of the $\Omega_1 \rightarrow \Omega_{10}$ flux and much less than half (16%) of the transport volume, as pointed out by *Holzer and Primeau* [2006], and as visible on the cumulative distributions $\int_0^\tau \phi d\tau'$ and $\int_0^\tau \mathcal{R} d\tau'$ of Figure 3.

[24] For residence times beyond τ_ϕ, the bulk of the $\Omega_1 \rightarrow \Omega_{10}$ path density moves further into the deep N Pacific, as seen in Figure 3 from the vertical integrals and Pacific zonal averages for 2410 and 3000 a. The zonal averages for each ocean basin at 1180, 2410, and 3000 a show that Ω_1-to-Ω_{10} waters in all basins move progressively deeper with increasing residence time. As the probability of having made contact with the surface at places other than Ω_{10} increases, the $\Omega_1 \rightarrow \Omega_{10}$ paths are forced to move ever deeper. The patterns shown for $\tau = 3000$ a capture 90% of the flux and 77% of the corresponding transport volume, and the cumulative distributions ($\int_0^\tau \phi d\tau'$ and $\int_0^\tau \mathcal{R} d\tau'$) can be seen to gradually approach 100% as τ increases beyond 3000 a. The asymptotic nature of the long-τ path density will be examined in detail in the next section.

[25] The plots in the bottom row of Figure 3 show the $\Omega_1 \rightarrow \Omega_{10}$ path density integrated over all residence times as a convenient summary of the overall spatial structure of η. The patterns resemble η at τ_ϕ combined with the long-τ deep-N-Pacific contribution. This reflects the fact that the residence-time integral effectively combines the patterns of η weighted by $\mathcal{R}(\tau, \Omega_1, \Omega_{10})$, which has a broad peak around $\tau \sim 1700$ a.

[26] Figure 4 shows the density of paths from Ω_1 to Ω_8 (the tropical Indian Ocean). Compared to the $\Omega_1 \rightarrow \Omega_{10}$ path densities, the timescale of the mode has decreased to $\tau_\phi = 470$ a (compare the ϕ versus τ curves of Figures 3 and 4), because the Ω_1-to-Ω_8 water does not make as lengthy a journey. The vertical integrals of Figure 4 for $\tau^{-}_{\phi/2} = 270$ a and $\tau_\phi = 470$ a show that the fast paths follow the conveyor routes to the Indian Ocean. The highest concentrations of Ω_1-to-Ω_8 waters occur near the Ω_8 surface at $\tau = \tau_\phi$, as they must (see the 470-a vertical integral and Indian-Ocean zonal average). The plots for $\tau = 3000$ a show that the small fraction of Ω_1-to-Ω_8 waters that survive for 3000 a and beyond are again found primarily in the deep N Pacific. The residence-time integrated patterns (not shown) combine the characteristics of the mode with those at long residence times as expected from the long tail of $\mathcal{R}(\tau, \Omega_1, \Omega_8)$ seen in the $\mathcal{R}$ versus τ curve.

[27] Figure 5 shows the density of paths connecting the N-Atlantic deep-water formation regions to the Southern Ocean. The corresponding transport is relatively fast with a mode at $\tau_\phi = 160$ a. For $\tau \sim \tau_\phi$ and shorter, the path density traces out the model's Atlantic deep western boundary current (see the vertical integrals for $\tau^{-}_{\phi/2} = 95$ a and $\tau_\phi = 160$ a). The evolution of the path density with residence time seen in the vertical integrals and the Atlantic zonal averages for $\tau = 95$, 160, and 350 a shows that with increasing residence time the Ω_1-to-Ω_5 waters spread

throughout the Atlantic and move to deeper depths for the same reasons as discussed for the $\Omega_1 \rightarrow \Omega_{10}$ case. The bulk of the Ω_1-to-Ω_5 waters are rapidly ventilated after a relatively short journey down the Atlantic. However, a tiny fraction of water (compare the maximum values, $\max_v$, of the vertical integral, or the values of $\int_0^\tau \mathcal{R} d\tau'$, for 3000 and 350 a) does leak into the Pacific via the deep Antarctic Circumpolar Current before being ultimately re-exposed in the Southern Ocean. The vertical integral and zonal averages for τ = 3000 a show that the straggler Ω_1-to-Ω_5 fluid elements that find themselves in the Pacific organize again in the deep N Pacific. Stragglers that did not escape the Atlantic are found in the deep N Atlantic.

3.1.2. Path Density of Waters Formed on the Southern Ocean Surface

[28] Most of the world's deep water, at least for our model, is formed on Ω_5, with $\mathcal{V}(\Omega_5, \Omega)/V$ = 58%. The bulk of this volume is re-exposed to the atmosphere on Ω_5, with $\mathcal{V}(\Omega_5, \Omega_5)/V$ = 28%. The other primary re-exposure regions are the tropical eastern Pacific (Ω_{10}), the tropical Indian Ocean (Ω_8), and the tropical Eastern Atlantic. Because our patch tiling does not resolve the eastern portion of the tropical Atlantic (Ω_3 covers all of the tropical Atlantic), and for economy of presentation, we restrict ourselves to the Ω_5, Ω_8, and Ω_{10} re-exposure regions that where examined for Ω_1 water in the previous subsection. The total residence-time-integrated $\Omega_5 \rightarrow \Omega_5$ flux is infinite in the continuum limit, because entry and exit patches overlap [*Primeau and Holzer*, 2006]. The total fluxes from Ω_5 to the other patches considered here are $\Phi(\Omega_5, \Omega_{10})$ = 2.8 Sv, and $\Phi(\Omega_5, \Omega_8)$ = 1.8 Sv, with corresponding total transport volume fractions of $\mathcal{V}(\Omega_5, \Omega_{10})/V$ = 7.1%, and $\mathcal{V}(\Omega_5, \Omega_8)/V$ = 4.2% [*Primeau and Holzer*, 2006]. These volume transports are of the same order of magnitude as tracer-based estimates of deep-water formation rates in the Southern Ocean [e.g., *Orsi et al.*, 2001]. However, a quantitative comparison is not meaningful because traditional tracer-based estimates of ventilation do not properly capture the effects of mixing, which can only be accounted for unambiguously by estimating the entire ventilation-rate distribution [*Primeau and Holzer*, 2006; *Hall et al.*, 2007].

[29] Figure 6 shows the paths from the Southern Ocean to the tropical eastern Pacific surface, Ω_{10}. As can be seen in the plot of ϕ versus τ, the $\phi(\tau, \Omega_5, \Omega_{10})$ distribution is nearly bimodal for this transport, with a fast mode at τ_ϕ = 76 a, and a plateau from $\tau \sim$ 800 to $\sim$1300 a followed by a long tail. The dashed line on the same plot shows that the corresponding transport-volume distribution $\mathcal{R} \sim \tau\phi$ is bimodal. The fast mode corresponds to Antarctic Intermediate water being transported along the coast of Chile by the wind-driven Peru current (see the evolution of the vertical integral and the Pacific zonal average for τ = 28, 76, and 200 a), while the plateau in ϕ (and dominant mode of $\mathcal{R}$) represents the slow spreading of Antarctic Bottom Water to the Pacific and Indian Oceans (this is particularly clear from the patterns for $\tau \sim$ 1700 a, not shown). The plots for $\tau \sim$ 3000 a show that the long-residence-time stragglers are again organized into the deep North Pacific in much the same pattern as the $\Omega_1 \rightarrow \Omega_{10}$ stragglers seen in the 3000-a plots of Figure 3.

[30] The $\Omega_5 \rightarrow \Omega_8$ path density from the Southern Ocean to the surface of the tropical Indian Ocean is shown in Figure 7. Similar to the $\Omega_5 \rightarrow \Omega_{10}$ paths, the corresponding flux-density distribution has a sharp peak at early times with τ_ϕ = 82 a, followed by a long tail (see the ϕ versus τ plot). The transport-volume distribution has a broad peak at $\tau \sim$ 1240 a (see the $\mathcal{R}$ versus τ plot). The plots of the vertical integral and Pacific zonal average for $\tau^-_{\phi/2}$ = 45 a and τ_ϕ = 82 a show that for $\tau \lesssim \tau_\phi$, the path density is organized primarily by the wind-driven gyre circulation. Paths organized by the South-Pacific subtropical gyre reach the Indian Ocean via the Indonesian throughflow. The region of high path density off the Australian east coast seen in the vertical integrals is due to the northward flowing deep western boundary current at depths greater than 800 m. Deeper transport through the Indian Ocean dominates for paths with intermediate residence times, $\tau \sim \tau^+_{\phi/2}$, as can be seen from the Indian Ocean zonal average at τ = 310 a. The long-residence-time stragglers at τ = 3000 a are organized into the deep N Pacific.

[31] Nearly half the water that had last surface contact on the Southern Ocean surface is re-exposed to the atmosphere over the Southern Ocean. Figure 8 shows the $\Omega_5 \rightarrow \Omega_5$ path densities at the 25% and 50% percentiles ($\tau_{25\%}$ = 290 a and $\tau_{50\%}$ = 1070 a) of the transport-volume distribution $\mathcal{R}(\tau, \Omega_5, \Omega_5)$ as well as at τ = 3000 a. In the zonal averages for $\tau_{25\%}$ = 290 a, the path density, or equivalently the density of waters with that residence time, displays distinct lobes corresponding to Antarctic Intermediate Water. The 290-a Atlantic zonal average also shows Antarctic Bottom Water. By $\tau_{50\%}$ = 1070 a, Ω_5-to-Ω_5 waters have spread to the deep Indian and Atlantic Oceans, as evident from the corresponding zonal averages. By τ = 3000 a, the remaining stragglers are again organized primarily into the deep N Pacific, although the zonal averages show that long-residence-time Ω_5-to-Ω_5 water also lingers in the deep Atlantic and Indian Oceans.

[32] In Figure 8 for $\Omega_5 \rightarrow \Omega_5$ transport, we again include the τ-integrated path density because it shows the dominance of short-τ paths for the case of overlapping (in this case coincident) entry and exit patches. The τ-integrated zonal averages show that the largest path density lies immediately under the Ω_5 surface. This reflects a $\Omega_5 \rightarrow \Omega_5$ flux-density distribution, $\phi(\tau, \Omega_5, \Omega_5)$, that diverges at $\tau = 0$ due to fluid elements that exit immediately after entry [*Primeau and Holzer*, 2006].

4. Long-Residence-Time Path Density

[33] At τ = 3000 a, the path densities seen in Figures 3–8 have strong similarities, suggesting that an asymptotic limit is being approached. We therefore systematically investigated the path density at τ = 3800 a (the longest residence time available from our simulations) for waters formed at the main deep-water formation regions of Ω_1 (North Atlantic) and Ω_5 (Southern Ocean), destined for each of the other patches, and also for the entire Ocean surface, Ω. [Note that $\eta(\mathbf{r}, \tau, \Omega_i, \Omega) = \Sigma_{f=1}^{11} \eta(\mathbf{r}, \tau, \Omega_i, \Omega_f)$]. We found that the patterns of the 3800-a path densities depend on whether the transport takes place primarily within the Atlantic or interconnects different basins, but that they are otherwise very similar. Representative examples are shown in Figure 9: The patterns of Ω_1 and Ω_5 waters destined for Ω_3 (top of Figure 9) are representative of the path densities whose destination patch lies in the North and Equatorial

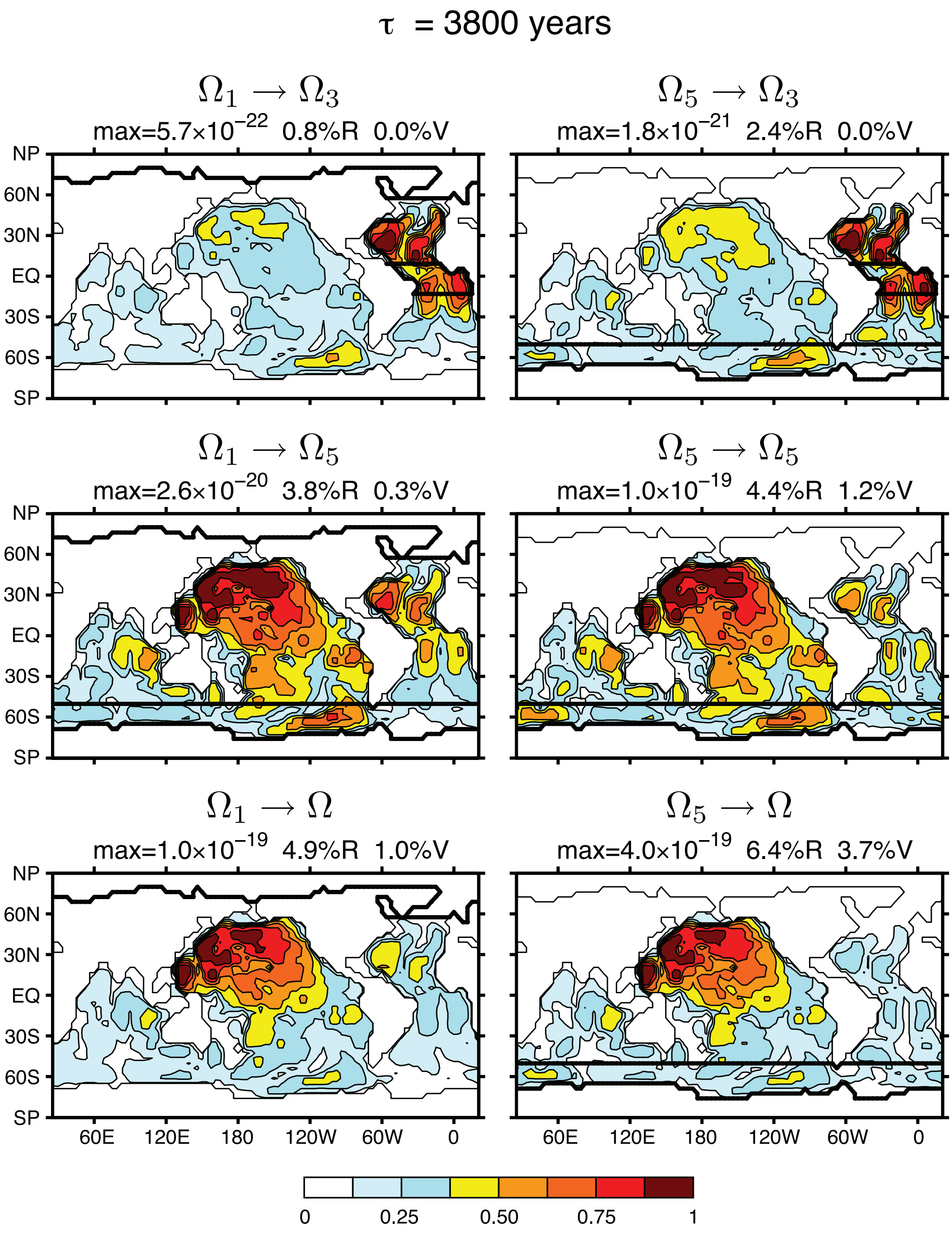
τ = 3800 years
Ω1 → Ω3
max=5.7×10−22 0.8%R 0.0%V
Ω5 → Ω3
max=1.8×10−21 2.4%R 0.0%V
Ω1 → Ω5
max=2.6×10−20 3.8%R 0.3%V
Ω5 → Ω5
max=1.0×10−19 4.4%R 1.2%V
Ω1 → Ω
max=1.0×10−19 4.9%R 1.0%V
Ω5 → Ω
max=4.0×10−19 6.4%R 3.7%V
NP
60N
30N
EQ
30S
60S
SP
60E
120E
180
120W
60W
0
0
0.25
0.50
0.75
1

Figure 9. The vertically integrated path density at τ = 3800 a for waters formed on the N-Atlantic surface, Ω_1, and Southern Ocean surface, Ω_5, destined to be re-exposed on Ω_3 (tropical Atlantic), Ω_5, and on the entire ocean surface, Ω. The entry and exit patches are outlined by heavy black lines. Each field has been divided by its maximum value, indicated in units of $m^{-2}\ a^{-1}$. The percentage %R indicates the fraction of $\Omega_i \rightarrow \Omega_f$ water with residence times greater than 3800 a, while %V is the percentage of the total ocean volume of this water. The contour interval is 0.125. The patterns of the path density of Ω_1 and Ω_5 waters destined for Ω_3 (top plots) are representative of the path densities of Ω_1 and Ω_5 waters destined for the North and Equatorial Atlantic ($\Omega_f = \Omega_1, \Omega_2, \Omega_3$), while the patterns of the path density of waters destined for Ω_5 (middle plots) are representative of inter-basin transport of Ω_1 and Ω_5 waters to destination patches $\Omega_f = \Omega_4, \ldots, \Omega_{11}$. See color plates if viewing the print version.

Atlantic ($\Omega_f = \Omega_1, \Omega_2, \Omega_3$), while the patterns of waters destined for Ω_5 (middle of Figure 9) are representative of inter-basin transport to destination patches $\Omega_f = \Omega_4, \ldots, \Omega_{11}$. The patterns of the path densities regardless of surface destination, that is, with $\Omega_f = \Omega$ (bottom of Figure 9), are seen to be dominated by interbasin paths, with little weight in the Atlantic and most of the long residence-time waters residing in the deep North Pacific.

[34] The plots of Figure 9 for Ω_1 and Ω_5 waters (the plots on the left and right, respectively) are strikingly similar: For a given exit patch it matters little at $\tau = 3800$ a whether the water originated on Ω_1 or Ω_5. This is a manifestation of the fact that waters that enter the interior through Ω_1 become blended with waters that enter through Ω_5 on a timescale short compared with 3800 a. The effect of this rapid blending is also visible in the patterns of the mean times since last Ω_1 and Ω_5 contact at 3185 m depth, which are nearly identical outside the Atlantic (see the plots of $\overline{\tau_\downarrow}$ in Figure 10).

[35] With increasing time since last surface contact, a fluid element's memory of its entry patch will be gradually erased by the action of diffusive mixing. Symmetrically, with increasing time to first contact with the exit patch, the action of diffusive mixing prevents the fluid element from "knowing" its eventual exit patch. (For the time reversed adjoint flow, this is can be thought of as a loss of memory of the exit patch.) Because very long residence time ultimately corresponds to both long time to first and long time since last contact, we expect that for asymptotically long τ surface-to-surface paths should become progressively more organized into a pattern that is universal in the sense of being independent of the entry/exit patch pair. The fact that at 3800 a the interbasin path densities (that is Ω_1 or $\Omega_5 \rightarrow \Omega_4, \Omega_5, \ldots, \Omega_{11}$) all have very similar patterns is evidence of this memory-loss effect. The bulk of the fluid elements tracing out the long-residence-time paths is organized into the deep N Pacific, with a characteristic pattern that we call the deep-N-Pacific (DNP) pattern.

[36] Figure 9 shows that for paths from the deep-water formation regions to the North or Equatorial Atlantic (that is Ω_1 or $\Omega_5 \rightarrow \Omega_1, \Omega_2$, or Ω_3), $\tau = 3800$ a is not long enough for the DNP pattern to manifest itself. Transport from Ω_1 or Ω_5 to Ω_1, Ω_2, or Ω_3 occurs efficiently within the Atlantic with very little water escaping to the other basins. What little fluid remains with $\tau = 3800$ a can be found predominantly in the abyssal N Atlantic. Fluid elements that journey from Ω_1 or Ω_5 to Ω_1, Ω_2, or Ω_3 can only organize into the dominant DNP pattern if they have sufficient time to be first transported to the deep N Pacific and then back to the Atlantic. Such fluid elements must follow deep-water paths to avoid surface contact before reaching their destination. The deep paths returning to the North or Equatorial Atlantic will be very slow, as they must either diffuse upstream in the southward flowing NADW or flow northward with the abyssal flow of the AABW. It is important to note that the low probability of such long-residence-time paths is reflected by the fact that less than 0.1% of the total ocean volume (the percentages are indicated in Figure 9) is ventilated by paths with $\tau > 3800$ a connecting Ω_1 or Ω_5 to the North and Equatorial Atlantic.

[37] The ultimate long-τ asymptotic fate of the path density follows from the asymptotic behavior of $\mathcal{G}$ and $\tilde{\mathcal{G}}$. As shown in Appendix D, as $\tau \rightarrow \infty$, the path density approaches η_∞ given by

$$\eta_\infty(\mathbf{r}, \tau, \Omega_i, \Omega_f) = e^{-\lambda_0 \tau}\left[\tau \alpha(\Omega_i, \Omega_f)\Psi(\mathbf{r}) + \Sigma(\mathbf{r}, \Omega_i, \Omega_f)\right], \quad (13)$$

where Ψ and Σ are τ-independent patterns defined in Appendix D in terms of the eigenvectors of the transport operator and its adjoint, and $\lambda_0 = (797 \text{ a})^{-1}$ is the smallest corresponding eigenvalue. The function $\Psi(\mathbf{r})$ in (13) is the asymptotic DNP pattern, because as $\tau \rightarrow \infty$, the asymptotic path density $\eta_\infty \rightarrow \alpha \tau e^{-\lambda_0 \tau}\Psi$. The DNP pattern, $\Psi(\mathbf{r})$, is plotted in Figure 11. Note that the DNP pattern carries no information on entry or exit patch, which means that the long-τ path density becomes asymptotically universal in the sense of independence on the choice of entry/exit patch pair, as we expect. The amplitude of the DNP pattern, $\alpha(\Omega_i, \Omega_f)\tau e^{-\lambda_0 \tau}$, does depend on where water enters and exits and governs the asymptotic fraction of water that finds its way into the deep N Pacific. The pattern $\Sigma(\mathbf{r}, \Omega_i, \Omega_f)$ of (13) represents the redistribution of the path density away from the ultimate DNP pattern. The bi-orthogonality of the eigenvectors of $\mathcal{G}$ and $\tilde{\mathcal{G}}$ (see Appendix D) guarantees that $\int d^3r\Sigma = 0$. Unlike the DNP pattern itself, Σ is non-universal because it does depend on the choice of entry/exit patch pair.

[38] Because both the amplitude of the DNP pattern, Ψ, and of the redistribution pattern, Σ, decay like $\exp(-\lambda_0 \tau)$, the $\tau\alpha\Psi$ term of (13) dominates Σ only linearly in τ. In other words, the redistribution corrections to the DNP pattern decay only like $1/\tau$. One can therefore expect corrections to the ultimate DNP pattern even if $\exp(-\lambda_0 \tau)$ has decayed substantially. Physically, the ultimate triumph of $\tau\alpha\Psi$ over Σ arises as follows: Fluid elements with very long τ are "lost" in the ocean interior and the integrated effect of quasi-random diffusive motion occurring for a long time ensures that the surface-to-**r** part of the paths becomes independent of the **r**-to-surface part of the paths. Therefore paths with all possible partitionings of τ into $\tau_\downarrow$ and $\tau_\uparrow = \tau - \tau_\downarrow$ become equally likely at very long τ. Consequently, the number of long-τ surface-to-surface paths, and hence their long-τ density, must be proportional to the number of ways τ can be partitioned into $\tau_\downarrow$ and $\tau_\uparrow$. The number of such partitions is proportional to τ. Thus for very long residence times η must not only decay exponentially with the spatial pattern of Ψ, but it must also be proportional to τ, that is, $\eta \propto \tau e^{-\lambda_0 \tau}\Psi$. It is only because of this extra factor of τ that the DNP contribution $\alpha \tau e^{-\lambda_0 \tau}\Psi$ ultimately dominates the redistribution corrections $e^{-\lambda_0 \tau}\Sigma$. Of course, if Σ has large amplitude for a given in/out patch pair, the DNP pattern may only come to dominate for residence times so long that the fraction of waters with such residence times, proportional to $\tau e^{-\lambda_0 \tau}$, is negligible.

[39] The asymptotic DNP pattern shown in Figure 11 has a general resemblance to the 3800-a inter-basin path densities, characteristic examples of which are shown in the $\Omega_1 \rightarrow \Omega_5$ and $\Omega_5 \rightarrow \Omega_5$ plots of Figure 9. However, there are quantitative differences, and the Atlantic intrabasin path densities from either Ω_1 or Ω_5 to Ω_1, Ω_2, or Ω_3 display hardly any weight in the deep N Pacific (see the $\Omega_1 \rightarrow \Omega_3$ and $\Omega_5 \rightarrow \Omega_3$ examples of Figure 9). We can understand the mismatch between the 3800-a path densities and the ulti-

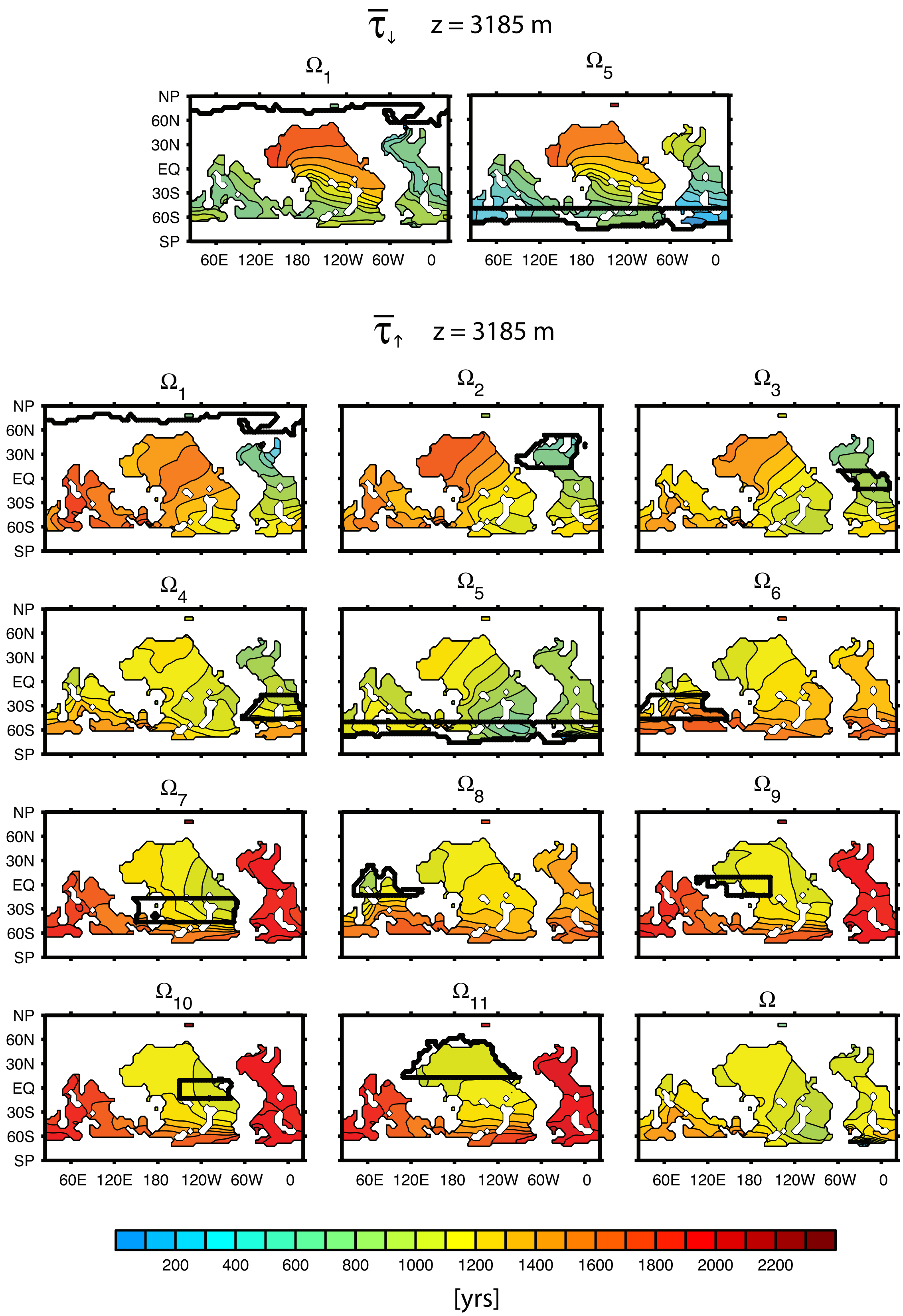
$\overline{\tau}_\downarrow$ z = 3185 m
Ω_1
Ω_5
NP
60N
30N
EQ
30S
60S
SP
60E 120E 180 120W 60W 0
$\overline{\tau}_\uparrow$ z = 3185 m
Ω_1
Ω_2
Ω_3
Ω_4
Ω_5
Ω_6
Ω_7
Ω_8
Ω_9
Ω_{10}
Ω_{11}
Ω
200 400 600 800 1000 1200 1400 1600 1800 2000 2200
[yrs]

Figure 10. The local mean time since last surface contact, $\overline{\tau_\downarrow}$, with Ω_1 and Ω_5 (two top plots), and the local mean time to first surface contact, $\overline{\tau_\uparrow}$, with each of the surface patches and with the entire ocean surface, Ω. All times are plotted at a depth of 3185 m and the entry patches (for $\overline{\tau_\downarrow}$) and exit patches (for $\overline{\tau_\uparrow}$) are outlined with heavy black lines. The contour interval is 100 a. See color plates if viewing the print version.

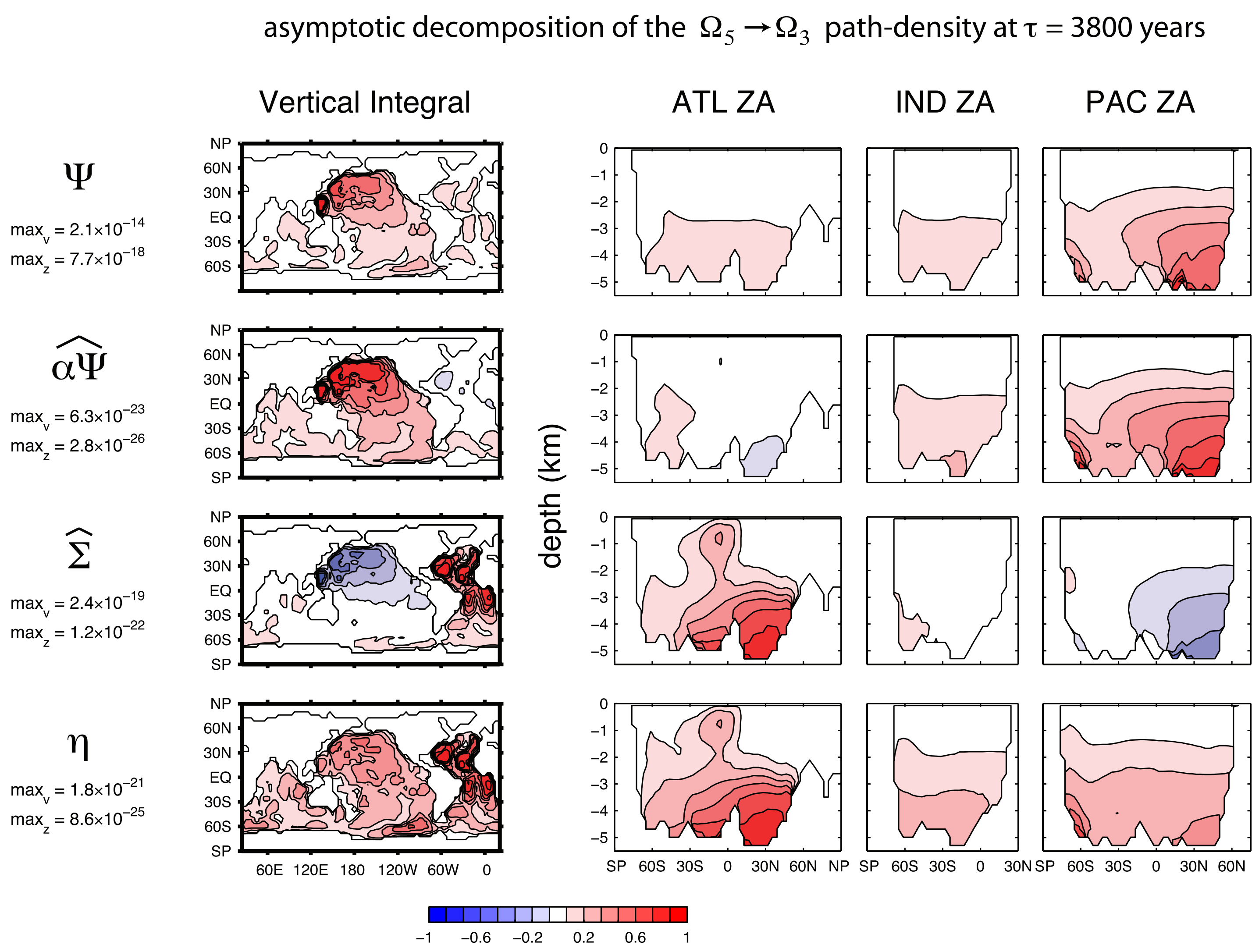

Figure 11. The top row of plots shows Ψ, the product of the longest lived eigenvector of the transport operator and that of its adjoint. This is the DNP pattern ultimately approached by the path density for very long τ. The second and third rows of plots show our estimates of $\widehat{\alpha\Psi}$ and $\widehat{\Sigma}$ for the $\Omega_5 \rightarrow \Omega_3$ path density (Southern Ocean to tropical Atlantic) obtained as described in the text. The bottom row shows plots of the $\Omega_5 \rightarrow \Omega_3$ path density $\eta = e^{-\lambda_0\tau}\,(\tau\widehat{\alpha\Psi} + \widehat{\Sigma})$. The vertical integrals have been normalized by their maximum value, $\max_v$, and the zonal averages have been normalized by their maximum value over all three basins, $\max_z$. The units of $\max_v$ are $m^{-2}\ a^{-1}$, and the units of $\max_z$ are $m^{-3}\ a^{-1}$. The contour interval is 0.133. See color plates if viewing the print version.

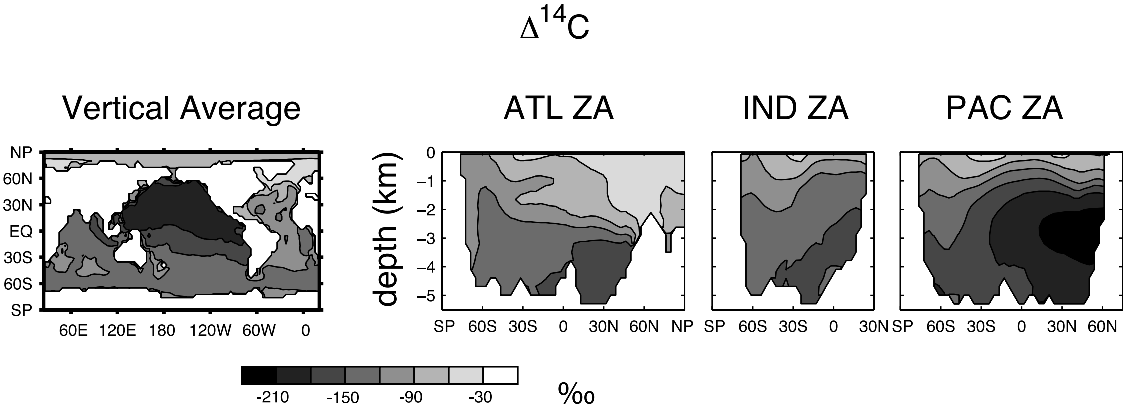

Figure 12. Simulated distribution of $\Delta^{14}C \equiv {}^{14}C/{}^{14}C_{\mathrm{atm}} - 1$ obtained by solving $\nabla \cdot [\rho\mathbf{u} - \rho\mathbf{K}\nabla]^{14}C = -\rho^{14}C/\tau_{14}$, where τ_{14} = 8267 a (a half-life of 5730 a), subject to a surface boundary condition that restores ^{14}C to a constant $^{14}C_{\mathrm{atm}}$ in the top 50-m-thick model level with a timescale τ_{as}. Following *Broecker and Peng* [1982], we use τ_{as} = 10 a. Because we plot only the ratio $^{14}C/^{14}C_{\mathrm{atm}}$, the actual value of the constant $^{14}C_{\mathrm{atm}}$ does not matter. The contour interval is 30 per mil.

mate asymptotic pattern of Ψ from equation (13). In order for η to be given by the asymptotic form (13), the amplitudes of the higher-order eigenvectors of $\mathcal{G}$ and $\widetilde{\mathcal{G}}$ must have decayed compared to the amplitude of the gravest eigenvector (that is, the eigenvector with the smallest eigenvalue, λ_0). For this to be the case, it is necessary that $\exp[-\tau(\lambda_1 - \lambda_0)] \ll 1$, which is satisfied with $(\lambda_1 - \lambda_0)^{-1}$ = 920 a for τ = 3800 a. Thus (13) is valid at τ = 3800 a and whether the DNP pattern is manifest or not depends on whether $\tau\alpha\Psi \gg \Sigma$, which we can check by estimating $\tau\alpha\Psi$ and Σ. Assuming $\eta = \eta_\infty$ exactly, and given η at two values of τ, we can regard (13) as an equation for the two unknowns $\alpha\Psi$ and Σ. Because (13) will not be exactly satisfied for any finite τ, this only provides estimates of $\alpha\Psi$ and Σ, which we denote by $\widehat{\alpha\Psi}$ and $\widehat{\Sigma}$.

[40] In Figure 11 we show an example of the decomposition of η into contributions from Ψ and Σ for the interesting case of the $\Omega_5 \rightarrow \Omega_3$ path density for which the DNP pattern has yet to manifest itself. The decomposition was obtained using η at τ = 3700 and 3800 a. The fact that the pattern of $\widehat{\alpha\Psi}$ approximates that of Ψ reasonably well confirms that (13) is approximately satisfied at τ = 3800 a. Furthermore, an estimate of α obtained by volume integrating $\eta/[\tau\exp(-\lambda_0\tau)]$ at τ = 3800 a yields a value within 3% of $\alpha = a_0(\Omega_5)\widetilde{a}_0(\Omega_3)/V$ obtained by calculating the coefficients a_0 and $\widetilde{a}_0$ directly by projecting $\mathcal{G}$ and $\widetilde{\mathcal{G}}$ onto the eigenvectors $\widetilde{\psi}_0$ and ψ_0, respectively. We are thus assured to have a reasonable estimate of the time-invariant re-distribution pattern $\Sigma(\mathbf{r}, \Omega_3, \Omega_5)$. In the N Pacific at 3185-m depth, the ratio $\tau\widehat{\alpha\Psi}/\widehat{\Sigma}$ is ~0.5, so that the DNP pattern cannot yet dominate Σ at τ = 3800 a. (A similar calculation based on η at 2900 and 3000 a, shows that (13) is not yet satisfied at 3000 a, indicating that the higher-order eigenvectors of the propagators have substantial amplitudes for $\Omega_3 \rightarrow \Omega_5$ transport.)

5. A New Picture of Global Deep-Water Paths and Implications for Natural ^{14}C

[41] The "Great Ocean Conveyor" [*Broecker*, 1991] has become an entrenched paradigm [e.g., *Colling et al.*, 2004; *Bradley*, 1999; *Albaréde*, 2003] of the global interbasin circulation. The picture of a Great Ocean Conveyor (GOC) is largely based on the observed distributions of long-lived tracers, whose structure is in turn often discussed in terms of the GOC. For example, the depletion of radiocarbon (^{14}C) in the deep N Pacific has been interpreted as locating the terminus of the GOC's deep branch [*Matsumoto and Key*, 2004; *England and Maier-Reimer*, 2001], where lengthy deep-waters routes first connect back to the upper-ocean circulation. However, in light of our path-density diagnostics, the notion of the large-scale circulation comprising an advective conveyor must be substantially modified to include the important effects of eddy-diffusive transport on long-lived tracers.

[42] Our path densities have shown that a significant fraction of the deep waters formed in the high-latitude oceans avoid being quickly transported by the ocean's current systems to their key re-exposure regions. Less than half of the transport from the N-Atlantic deep-water formation regions to the tropical eastern Pacific follows the classical GOC. The majority of the transport occurs via a "diffusive conveyor" [*Holzer and Primeau*, 2006]. The diffusive conveyor is composed of water that "falls off" the conveyor belt (current systems) through the action of turbulent eddies and larger-scale recirculating gyres. This water may become re-entrained into the current systems (possibly falling off and being re-entrained multiple times), or it may get "lost" entirely in the stagnant parts of the ocean. On the basin scale, the deep N Pacific is the most stagnant part of the ocean and, therefore, not accessible via the major current systems. Instead, transport into the deep N Pacific must occur via the effectively diffusive action of eddies and/or slow, shear-dispersive abyssal flows. Such processes are absent from the traditional GOC picture, and in our model they are parameterized as diffusive mixing.

[43] Our new picture of the surface-to-surface transport provides a natural interpretation of the structure of ^{14}C that is more physical than the postulate of a GOC terminus. To illustrate this point, we have simulated natural ^{14}C using our model. Basing our discussion on the simulated ^{14}C distribution ensures that our interpretation is consistent with the

model's path densities. Figure 12 shows the simulated ^{14}C in terms of the usual $\Delta^{14}C \equiv {}^{14}C/{}^{14}C_{\mathrm{atm}} - 1$, where ^{14}C is the local concentration of ^{14}C in the ocean, and $^{14}C_{\mathrm{atm}}$ is the concentration in the lower atmosphere. The model's Δ^{14}C distribution is broadly consistent with observations [e.g., *Matsumoto and Key*, 2004], having the greatest depletion in the N Pacific at a depth of ~2500 m.

[44] A rough carbon age can be estimated as $\tau_C = \tau_{14}\log[(1 + \Delta^{14}C)/(1 + \Delta^{14}C_s)]$, where τ_{14} = 8267 a is the radioactive *e*-folding decay time, and $\Delta^{14}C_s$ is an appropriate surface value. With $\Delta^{14}C_s \sim 85$ per mil (the N-Atlantic and Southern-Ocean averages), and a deep N-Pacific value of ~210 per mil, one obtains $\tau_C \sim 1200$ a. In the conventional GOC picture, this would be the time for which newly formed deep waters ride the conveyor to its N Pacific terminus, where they are promptly returned to the surface.

[45] Our diagnostics show, however, that this GOC interpretation of the Δ^{14}C structure is wrong in several aspects. First, our ventilation-rate diagnostics [*Primeau and Holzer*, 2006] have shown that the model's deep water is primarily returned to the mixed layer in the equatorial upwelling regions and the Southern Ocean, and not in the N Pacific. Additionally, much of the world's deep water is not only formed in the N Atlantic, but also in the Southern Ocean. These findings corroborate other recent work on oceanic transport [e.g., *Schmitz*, 1995; *Toggweiler and Samuels*, 1993; *Sun and Bleck*, 2001; *Ganachaud and Wunsch*, 2000]. Second, newly formed deep waters are not advected in stately fashion along the ocean's major current systems. Instead, the advective paths from the N-Atlantic to the tropical eastern Pacific are only discernable for times less than the mode of the corresponding flux distribution at ~1200 a (Figure 3). Advective paths from the Southern Ocean to the Pacific re-exposure regions are several times faster still (Figure 6). The corresponding ϕ and $\mathcal{R}$ distributions show that the fast paths to the re-exposure regions carry significantly less than half the associated flux and transport volume.

[46] The depletion of ^{14}C in the deep N Pacific does not represent a simple advective conveyor timescale. A water parcel in the deep N Pacific is composed of fluid elements whose distribution $\mathcal{G}(\mathbf{r}, \tau_\downarrow|\Omega)$ of times $\tau_\downarrow$ ("ideal ages") since last surface contact, is very broad with a long tail for large $\tau_\downarrow$. The ^{14}C concentration represents a mixture of a minority of young, less depleted waters with a long tail of older, more depleted waters. In fact, the concentration of radiocarbon in the interior, ^{14}C, is given by $^{14}C(\mathbf{r}) = {}^{14}C_s\int_0^\infty \mathcal{G}(\mathbf{r}, \tau_\downarrow|\Omega)e^{-\tau_\downarrow/\tau_{14}}d\tau_\downarrow$, to the approximation that spatial variations in the mixed-layer radiocarbon concentration can be neglected. Thus to first order in the mean ideal age, $\overline{\tau_\downarrow}(\mathbf{r}) \equiv \int_0^\infty \mathcal{G}(\mathbf{r}, \tau_\downarrow|\Omega)\tau_\downarrow d\tau_\downarrow$, we have $\Delta^{14}C \sim [{}^{14}C(\mathbf{r}) - {}^{14}C_s]/{}^{14}C_s \sim -\overline{\tau_\downarrow}(\mathbf{r})/\tau_{14}$, so that we expect $\Delta^{14}C$ to have a structure qualitatively similar to $\overline{\tau_\downarrow}$, which is in fact the case [for plots of $\overline{\tau_\downarrow}$, see the work of *Primeau*, 2005, where $\overline{\tau_\downarrow}$ is denoted by Γ]. In the region of the maximum ^{14}C depletion, the mean time since last contact anywhere with the mixed layer is $\overline{\tau_\downarrow} \sim 1600$ a. Although we will not pursue it here, a more complete analysis of the ^{14}C distribution, which allows for separate N-Atlantic and Southern-Ocean end-members is readily accomplished by using the fact that at depth $\mathcal{G}(\mathbf{r}, \tau_\downarrow|\Omega) \sim \mathcal{G}(\mathbf{r}, \tau_\downarrow|\Omega_1) + \mathcal{G}(\mathbf{r}, \tau_\downarrow|\Omega_5)$, with negligible contributions from the other surface patches [*Primeau*, 2005].

[47] Our transport diagnostics thus paint a picture of ^{14}C being transported into the stagnant deep N Pacific primarily by eddy-diffusive and shear-dispersive transport that is characterized by strong mixing giving the boundary propagators, $\mathcal{G}(\mathbf{r}, \tau_\downarrow|\Omega_i)$, long tails in $\tau_\downarrow$. Our diagnostics additionally show that not only does it take a long time to transport deep-water into the deep N Pacific, it also takes a long time for this water to be re-exposed to the atmosphere. The mean time for water in the deep N Pacific to be re-exposed to the atmosphere, $\overline{\tau}_\uparrow$, at each of the 11 surface patches, is shown in Figure 10. In the deep N Pacific (z = 3185 m) the mean time to be re-exposed to the atmosphere is ~1100 a and can range from 900-1800 a depending on the exit patch. We therefore interpret the pattern of Δ^{14}C as identifying the deep N Pacific not as the terminus of the interbasin circulation, but as the ocean's "holding pen" in which about half of the world's deep waters with residence times of more than ~2000 a are found. [The 50% quantiles of $\mathcal{R}(\tau, \Omega_1, \Omega_{10})$ and $\mathcal{R}(\tau, \Omega_5, \Omega_{10})$ are both at ~2000 a.] Both entry and exit into this relatively stagnant holding pen can only occur through slow eddy-diffusive transport in a coarse-grained description of the ocean.

6. Discussion and Conclusions

[48] We have developed a new transport diagnostic for the joint density in space and residence time of advective-diffusive surface-to-surface paths. The diagnostic identifies the paths connecting a specified entry patch with a specified exit patch and partitions these paths according to the patch-to-patch transit time, which is the residence time in the ocean interior. The spatially integrated path density gives the associated flux and transport-volume distributions introduced by *Primeau and Holzer* [2006] to characterize ventilation rates. The path density thus not only identifies the pathways, but also quantifies the transport carried along the paths.

[49] It is important to emphasize that the path-density diagnostic differs in a number of important ways from the traditional stream function of the meridional overturning circulation (MOC). The MOC stream function is a purely advective diagnostic that is a useful index of the circulation strength, but it does not capture the diffusive transport due to turbulent eddies. As such, the MOC stream function does not describe the transport of any tracers. The MOC stream function represents recirculation primarily within the interior of the Atlantic, whereas the path density captures transport through the interior that connects surface patches. The fluxes associated with the path density can be interpreted as formation rates and quantify the flow rate of the surface-to-surface transport. By contrast, the strength of the MOC should not be interpreted as a formation rate, and certainly not as the flow rate of the global conveyor.

[50] The utility of the path-density diagnostic has been demonstrated using a global steady state ocean model [*Primeau*, 2005]. Our results quantify the structure of the ocean's deep-water paths and paint a new picture of their character. Advective conveyor-type routes from the deep-water formation regions to the equatorial and Southern-Ocean re-exposure regions characterize only the fastest paths with residence times less than the mode of the flux distribution ϕ. These fast path account for significantly less

than half of the total patch-to-patch flux and transport volume. Paths with residence times longer than the mode of ϕ become progressively more diffuse due to the action of eddies and shear dispersion. For residence time $\tau \sim 3000$ a, the density of interbasin paths is organized into the deep N Pacific, with only weak dependence on the choice of entry/exit patch pair. The observed structure of long-lived tracers such as radio carbon is consistent with the deep N Pacific being a stagnant holding pen of long-residence-time waters that are characterized by both long mean times since last surface contact and long mean times to subsequent re-exposure. Because of its stagnant nature, access to the deep N Pacific is dominated by diffusive transport in a coarse-grained description of the ocean. The deep N Pacific should therefore not be regarded as a terminus of an advective conveyor, but instead as a holding pen of the "diffusive conveyor."

[51] For long residence times, τ, the path density ultimately approaches the Deep-North-Pacific (DNP) pattern set by the slowest decaying (gravest) eigenmodes of the transport operator and its adjoint. Because the eigenmodes depend only on the transport operator and the homogeneous zero-concentration boundary condition at the surface, the DNP pattern is independent of the entry and exit locations of the paths. However, even at $\tau = 3800$ a, or approximately at 4.8 e-foldings of the gravest eigenmode, the DNP pattern is not yet manifest for paths starting and ending in the Atlantic, and even inter-basin paths show some deviations from the DNP pattern. The reasons for this surprisingly slow convergence of η to the ultimate DNP pattern was revealed through a detailed exploration of the long-τ asymptotics. While the path density decays exponentially with the longest-lived eigenmode of the transport operator, the pattern multiplying this exponential consists of the sum of the time-invariant, entry/exit-patch independent DNP pattern with an amplitude proportional to τ, and a time-invariant, zero-mean redistribution pattern, Σ. Thus the DNP pattern wins over Σ only linearly with τ. For interbasin paths connecting the North Atlantic or Southern Ocean with the Pacific or Indian Ocean, the DNP pattern is beginning to emerge at $\tau \sim 3000$ a, and we verified that by $\tau = 3800$ a the path density is well approximated by the two-pattern asymptotic form. However, for paths connecting the North Atlantic or Southern Ocean with the North or tropical Atlantic, the DNP pattern is not yet manifest at $\tau = 3800$ a because of the substantial amplitude of the entry/exit-patch dependent redistribution pattern, Σ. For these paths very large τ will be required before the path density approximates the DNP pattern. The corresponding fraction of the ocean with such long residence time will be negligible due to the overall exponential decay.

[52] Our picture of the oceanic surface-to-surface paths has been deduced on the basis of a coarse-resolution model. This is in itself of value given that our model is typical of those used for biogeochemical studies. An obvious question is whether we can extrapolate our findings to the real ocean. After all, the coarse resolution used necessitates high eddy diffusivities and one might be tempted to argue that things would be different had we been able to integrate an eddy-permitting model for several thousand years.

[53] There are good reasons to believe that the qualitative features of our picture of surface-to-surface transport are robust and also characteristic of the real ocean. A high-resolution model with a reduced explicit eddy-diffusivity would contain resolved eddies, and the effect of such quasi-random eddy motion on dispersal and mixing is diffusive on average. Eddy-resolving models would also produce more sharply defined boundary currents with stronger shear flows, and the effect of such enhanced shear is to increase tracer dispersion. Heuristic arguments aside, the point of view that the real ocean is in a regime of strong mixing is supported by analyses of simultaneous measurements of CFC's and/or tritium and helium [*Jenkins*, 1988; *Robbins et al.*, 2000; *Waugh et al.*, 2004]. All these studies estimated that the effective Péclet number of the ocean is of order unity or less, implying strongly diffusive transport. *Waugh et al.* [2004] estimated the entire transit-time distribution, $\mathcal{G}$, using the combined information contained in CFC, helium, and tritium data and found that $\mathcal{G}$ is broad with a long tail, implying that there is substantial mixing of waters with different ages in the ocean. More importantly, the ratio of the width to the mean of $\mathcal{G}$ as estimated by *Waugh et al.* [2004] is in the range of 0.75 to 1.25, again implying strongly diffusive transport. At first, these findings appear to be at odds with one's view that the real ocean is in a highly non-diffusive regime. However, it must be kept in mind that (a) even a weak micro-scale diapycnal diffusivity will lead to substantial mixing if it acts for a long time, and that (b) the long-τ tails of $\mathcal{G}$ and of the path density are diffusive not in the sense of being due to a large micro-scale iso- and/or diapycnal diffusivity, but in the sense of resulting from the average effect of quasirandom advective dispersal by turbulent eddies and shears on all scales.

[54] Some aspects of our "diffusive conveyor" picture are likely to be model dependent. For example, the relative fraction of the ocean volume that is ventilated by different surface-to-surface pathways is likely to be sensitive to the model's representation of deep-water formation in the North Atlantic and Southern Ocean. Since the dynamical processes involved in deep-water formation are unresolved in our model, our picture is unlikely to be quantitatively correct. The precise timescales associated with our surface-to-surface transit-time distributions are also likely to change in higher resolution models. The more vigorous boundary currents of higher-resolution models are expected to speed up the fast advective surface-to-surface paths. However, the decreased explicit diffusion would decrease the volume fraction ventilated by the very fastest advective-diffusive paths. The effect of a weaker explicit diffusivity on the slow paths is difficult to predict because of the compensating effects of the expected increase in eddy activity. Models with higher resolution can also better represent bottom topography that can support stronger topographically trapped abyssal currents as well as poorly ventilated dead zones. We speculate that the combined effects of these topographic effects will be to broaden the distribution of surface-to-surface transport even further and, therefore, to enhance the diffusive nature of the modeled conveyor. However, the quantitative effects of higher resolution and correspondingly reduced explicit diffusivities are unknown. It will be interesting to repeat our diagnostics with higher resolution models once the compu-

tational resources become available. We are currently investigating alternative computational methods for estimating η that do not rely on the use of an adjoint model in the hope of making our diagnostic framework more widely accessible.

[55] Our diagnostic shows that a substantial part of the ocean can be ventilated eddy-diffusively along isopycnals. This illustrates that quasi-horizontal mass transport to regions of localized enhanced vertical mixing can reconcile the requirement of a substantial globally averaged diffusivity [*Munk and Wunsch*, 1998] with micro-structure measurements [e.g., *Toole et al.*, 1994] that do not find the required mixing in the interior. An interesting future research application of our diagnostic is to determine the sensitivity of surface-to-surface paths to the nature of the vertical mixing by computing the path density for models that assume essentially zero diapycnal mixing in the interior [e.g., *Marotzke*, 1997; *Toggweiler and Samuels*, 1998].

[56] We anticipate that our path-density diagnostic will be useful for analyzing the transport of a variety of oceanic tracers. An immediate application is to diagnose the surface-to-surface pathways of preformed nutrients. Our diagnostic will help us understand how unused nutrients in one part of the ocean can be transported below the euphotic zone to fertilize other parts of the near-surface ocean. The ocean's most fundamental scalar quantities are temperature and salinity, and we also plan to extend the path-density diagnostic so it is suitable for tracing the pathways of heat and salt. Finally, the diagnostic is applicable to any bounded fluid and we plan to use it to analyze the transport of constituents in the atmosphere.

Appendix A: Probabilistic Derivation of η

[57] A single fluid element, or particle for short, at point $(\mathbf{r}_0, t)$, that made last contact on Ω_i at time t_i and that will make first contact with Ω_f at time $t_f = t_i + \tau$, has a joint density in space and residence time of $\delta(\mathbf{r} - \mathbf{r}_0)\, \delta(t_f - t_i - \tau)\delta_{i,i_0}\delta_{f,f_0}$. The joint density of such particles in the fluid at $(\mathbf{r}_0, t)$ is obtained by averaging over the probablities of finding such a fluid element (see Figure 1):

$$\eta\left(\mathbf{r}_0, \tau, \Omega_{i_0}, \Omega_{f_0}; t\right) = \left\langle \delta(\mathbf{r} - \mathbf{r}_0)\delta\left(t_f - t_i - \tau\right)\delta_{i,i_0}\delta_{f,f_0}\right\rangle, \tag{A1}$$

where $\langle \ldots \rangle$ denotes the average at time t over the following probabilities:

[58] (a) The joint probability of times and places since last surface contact, that is, the joint probability that fluid at $\mathbf{r}$ had last contact with patch Ω_i at time t_i after a transit time in the interval $(t - t_i, t - t_i + dt_i)$:

$$\mathcal{G}(\mathbf{r}, t|\Omega_i, t_i)dt_i. \tag{A2}$$

[59] (b) The joint probability of times and places to first surface contact, that is, the joint probability that fluid at $\mathbf{r}$ will first make contact with patch Ω_f at time t_f after a transit time in the interval $(t_f - t, t_f - t + dt_f)$:

$$\widetilde{\mathcal{G}}\left(\mathbf{r}, t|\Omega_f, t_f\right)dt_f. \tag{A3}$$

[60] (c) The probability of finding fluid elements in the interior volume $d^3\mathbf{r}$ at $(\mathbf{r}, t)$:

$$\frac{\rho(\mathbf{r}, t)}{M} d^3\mathbf{r}, \tag{A4}$$

where M denotes the total mass of the ocean.

[61] With these probabilities η becomes

$$\eta\left(\mathbf{r}_0, \tau, \Omega_{i_0}, \Omega_{f_0}; t\right) = \tag{A5}$$

$$\sum_{i,f} \int_V d^3r \frac{\rho(\mathbf{r}, t)}{M} \int_{-\infty}^{t} dt_i \int_t^{\infty} dt_f \cdot \widetilde{\mathcal{G}}\left(\mathbf{r}, t|\Omega_f, t_f\right)\mathcal{G}(\mathbf{r}, t|\Omega_i, t_i)\delta(\mathbf{r} - \mathbf{r}_0)\delta\left(t_f - t_i - \tau\right)\delta_{i,i_0}\delta_{f,f_0}. \tag{A6}$$

Summing out the trivial Kronecker deltas and integrating out $\delta(\mathbf{r} - \mathbf{r}_0)$ and $\delta(t_{f_0} - t_{i_0} - \tau)$ over t_{f_0} gives

$$\eta\left(\mathbf{r}_0, \tau, \Omega_{i_0}, \Omega_{f_0}; t\right) = \frac{\rho(\mathbf{r}_0, t)}{M} \int_{t-\tau}^{t} dt_{i_0}\, \widetilde{\mathcal{G}}\left(\mathbf{r}_0, t|\Omega_f, t_{i_0} + \tau\right) \mathcal{G}\left(\mathbf{r}_0, t|\Omega_{i_0}, t_{i_0}\right). \tag{A7}$$

Integrating out t_{i_0} gives the same result and is equivalent to making the change of variables $t_{i_0} \rightarrow t_{f_0} - \tau$ in (A7).

Appendix B: Moments of η

[62] Making a change of variables to $\tau_\uparrow = t_f - t$ (time to exit from current location) and $\tau_\downarrow = t - t_i$ (time since entry), and leaving the delta function in time in expression (A6) for η, gives the most convenient starting point for calculating the moments of η:

$$\int_0^\infty d\tau\tau^n\eta = \frac{\rho(\mathbf{r}, t)}{M} \int_0^\infty d\tau \int_0^\infty d\tau_\downarrow \int_0^\infty d\tau_\uparrow \cdot \tau^n \widetilde{\mathcal{G}}\left(\mathbf{r}, t|\Omega_f, t + \tau_\uparrow\right)\mathcal{G}\left(\mathbf{r}, t|\Omega_i, t - \tau_\downarrow\right)\delta\left(\tau_\uparrow + \tau_\downarrow - \tau\right). \tag{B1}$$

Integrating over τ, and expanding the term $(\tau_\downarrow + \tau_\uparrow)^n$ resulting from τ^n using the binomial theorem, we obtain

$$\int_0^\infty d\tau\tau^n\eta = \frac{\rho(\mathbf{r}, t)}{M} \sum_{m=0}^{n} \binom{n}{m} \int_0^\infty d\tau_\uparrow \tau_\uparrow^{n-m} \widetilde{\mathcal{G}}\left(\mathbf{r}, t|\Omega_f, t + \tau_\uparrow\right) \cdot \int_0^\infty d\tau_\downarrow \tau_\downarrow^m \mathcal{G}\left(\mathbf{r}, t|\Omega_i, t - \tau_\downarrow\right), \tag{B2}$$

which we can write in terms of the normalized temporal moments of the boundary propagators as

$$\int_0^\infty d\tau\tau^n\eta = \frac{\rho(\mathbf{r}, t)}{M} \widetilde{f}\left(\mathbf{r}, t|\Omega_f\right) f\left(\mathbf{r}, t|\Omega_i\right) \cdot \sum_{m=0}^{n} \binom{n}{m} \overline{\tau_\uparrow^{n-m}\left(\mathbf{r}, t|\Omega_i\right)}\ \overline{\tau_\downarrow^m\left(\mathbf{r}, t|\Omega_f\right)}, \tag{B3}$$

where $\overline{\tau_\downarrow^m}(\mathbf{r}, t|\Omega_i) \equiv \int_0^\infty d\tau_\downarrow \tau_\downarrow^m \mathcal{G}(\mathbf{r}, t|\Omega_i, t - \tau_\downarrow)/f(\mathbf{r}, t|\Omega_i)$ is the mth moment of $\mathcal{G}$ and $\overline{\tau_\uparrow^{n-m}}(\mathbf{r}, t|\Omega_i)$ is the analogously defined $(n - m)$th moment of $\widetilde{\mathcal{G}}$, with $f(\mathbf{r}, t|\Omega_i) \equiv \int_0^\infty d\tau_\downarrow \mathcal{G}(\mathbf{r}, t|\Omega_i, t - \tau_\downarrow)$ and $\widetilde{f}(\mathbf{r}, t|\Omega_f) \equiv \int_0^\infty d\tau_\uparrow \widetilde{\mathcal{G}}(\mathbf{r}, t|\Omega_f, t + \tau_\uparrow)$.

[63] Of particular interest is the case $n = 0$, that is, the residence-time integrated path density:

$$\int_0^\infty d\tau\eta = \frac{\rho(\mathbf{r},t)}{M}\widetilde{f}\left(\mathbf{r},t|\Omega_f\right)f\left(\mathbf{r},t|\Omega_i\right). \tag{B4}$$

Thus

$$\overline{\tau^n} = \sum_{m=0}^{n}\binom{n}{m}\overline{\tau_\uparrow^{n-m}}\ \ \overline{\tau_\downarrow^m}, \tag{B5}$$

where we have suppressed the arguments for clarity, and $\overline{\tau^n} \equiv \frac{\int_0^\infty d\tau\tau^n\eta}{\int_0^\infty d\tau\eta}$. In particular, the local mean residence time ($n = 1$) of fluid undergoing the $\Omega_i \rightarrow \Omega_f$ journey is simply given by the sum of the mean time since last contact with Ω_i and the mean time to first contact with Ω_f, that is,

$$\overline{\tau\left(\mathbf{r},\Omega_i,\Omega_f;t\right)} = \overline{\tau_\downarrow(\mathbf{r},t|\Omega_i)} + \overline{\tau_\uparrow\left(\mathbf{r},t|\Omega_f\right)}. \tag{B6}$$

Appendix C: Derivation of $\mathcal{R}$ as Volume Integral of η

[64] The total volume of water per unit residence time in the ocean at time t that had last surface contact on Ω_i and that is on its way to Ω_f is obtained by integrating $\eta(\mathbf{r}, \tau, \Omega_i, \Omega_f; t)$ over the entire ocean:

$$\mathcal{R}\left(\tau,\Omega_i,\Omega_f;t\right) = \int_V d^3\mathbf{r}\ \eta\left(\mathbf{r},\tau,\Omega_i,\Omega_f;t\right)\ . \tag{C1}$$

Equation (C1) can be simplified by expressing the boundary propagators in the expression for η in terms of fluxes of the usual δ-function-source Green functions and exploiting the basic properties of these Green functions.

[65] The δ-function-source Green function, $G(\mathbf{r}, t|\mathbf{r}', t')$, obeys $\partial[\rho G(\mathbf{r}, t|\mathbf{r}', t')]/\partial t + [\rho\mathbf{u} - \rho\mathbf{K}\nabla]G(\mathbf{r}, t|\mathbf{r}', t') = \delta(\mathbf{r} - \mathbf{r}')\delta(t - t')$ subject to the homogeneous boundary condition $G = 0$ at the sea surface. The corresponding Green function for the time-reversed adjoint flow is given by the reciprocity condition $\widetilde{G}(\mathbf{r}, t|\mathbf{r}', t') = G(\mathbf{r}', t'|\mathbf{r}, t)$. In terms of G and $\widetilde{G}$, the boundary propagators are given by [*Holzer and Hall*, 2000]:

$$\mathcal{G}(\mathbf{r},t|\Omega_i,t_i) = -\int_{\Omega_i} d^2r_i\rho\widehat{n}\cdot\mathbf{K}^T\nabla_{\mathbf{r}_i}\widetilde{G}(\mathbf{r}_i,t_i|\mathbf{r},t), \tag{C2}$$

and

$$\widetilde{\mathcal{G}}\left(\mathbf{r},t|\Omega_f,t_f\right) = -\int_{\Omega_f} d^2r_f\rho\widehat{n}\cdot\mathbf{K}\nabla_{\mathbf{r}_f}G\left(\mathbf{r}_f,t_f|\mathbf{r},t\right). \tag{C3}$$

The subscripts on the gradients indicate the variable on which the gradients act. Subsituting these relationships into (C1), with η given by (A7), using the reciprocity relation, and applying the Chapman-Kolmogorov identity $\int_V d^3r\ \rho G(\mathbf{r}_A,\ t_A|\mathbf{r},\ t)G(\mathbf{r},\ t|\mathbf{r}_B,\ t_B) = G(\mathbf{r}_A,\ t_A|\mathbf{r}_B,\ t_B)$, the volume-integrated product $\mathcal{G}\ \widetilde{\mathcal{G}}$ in the integrant of η can be reduced to the flux of either only $\mathcal{G}$ or $\widetilde{\mathcal{G}}$. Expressions (7) and (8) are obtained after algebraic simplification.

Appendix D: Long-τ Asymptotic Path Density

[66] We limit ourselves to the steady state case here. The asymptotic expression for η in the limit of long τ is derived by expanding the boundary propagators in terms of the eigenvectors ψ and $\widetilde{\psi}$ of the transport operator:

$$\mathcal{G}\left(\mathbf{r},\tau_\downarrow|\Omega_i\right) = \sum_{m=0}^{\infty} a_m(\Omega_i)\psi_m(\mathbf{r})e^{-\lambda_m\tau_\downarrow}, \tag{D1}$$

and

$$\widetilde{\mathcal{G}}\left(\mathbf{r},\tau-\tau_\downarrow|\Omega_f\right) = \sum_{n=0}^{\infty}\widetilde{a}_n\left(\Omega_f\right)\widetilde{\psi}_n(\mathbf{r})e^{-\lambda_n\left(\tau-\tau_\downarrow\right)}, \tag{D2}$$

where $\tau_\downarrow = t - t_i$ and the eigenvectors are given by

$$\nabla\cdot[\rho\mathbf{u} - \rho\mathbf{K}\nabla]\psi_m = -\lambda_m\psi_m, \tag{D3}$$

and

$$\nabla\cdot\left[-\rho\mathbf{u} - \mathbf{K}^T\nabla\right]\widetilde{\psi}_n = -\lambda_n\widetilde{\psi}_n. \tag{D4}$$

(The homogeneous zero-concentration boundary condition is incorporated into the transport operator on the left.) Note that the eigenvectors of the forward and adjoint transport operators are bi-orthogonal, that is,

$$\int \psi_m(\mathbf{r})\widetilde{\psi}_n(\mathbf{r})\,d^3r = \delta_{m,n}. \tag{D5}$$

Substituting expansions (D1) and (D2) into expression (9) for η and integrating over $\tau_\downarrow$ gives (suppressing the arguments of the a's and ψ's for succinctness):

$$\eta = \frac{1}{V}\sum_{n=0}^{\infty}\widetilde{a}_na_n\widetilde{\psi}_n\psi_ne^{-\lambda_n\tau}\tau + \frac{1}{V}\sum_{n\neq m}^{\infty}\widetilde{a}_na_m\widetilde{\psi}_n\psi_m\frac{e^{-\lambda_m\tau} - e^{-\lambda_n\tau}}{\lambda_n - \lambda_m}. \tag{D6}$$

We now designate λ_0 to be the eigenvalue with the smallest real part. For the ocean λ_0 is purely real due to the presence of diffusive dissipation. Therefore in any sums of exponentials only terms proportional to $e^{-\lambda_0\tau}$ contribute for long τ, giving

$$\eta \simeq \frac{1}{V}\widetilde{a}_0a_0\widetilde{\psi}_0\psi_0e^{-\lambda_0\tau}\tau + \frac{1}{V}\sum_{n=1}^{\infty}\left(\widetilde{a}_n\widetilde{\psi}_na_0\psi_0 + a_n\psi_n\widetilde{a}_0\widetilde{\psi}_0\right)\frac{e^{-\lambda_0\tau}}{\lambda_n - \lambda_0}. \tag{D7}$$

With the definitions

$$\Psi(\mathbf{r}) \equiv \widetilde{\psi}_0(\mathbf{r})\psi_0(\mathbf{r}), \tag{D8}$$

which we call the deep-N-Pacific (DNP) pattern,

$$\Sigma(\mathbf{r},\Omega_i,\Omega_f) \equiv \frac{1}{V}\sum_{n=1}^{\infty}\Big(\widetilde{a}_n(\Omega_f)\widetilde{\psi}_n(\mathbf{r})a_0(\Omega_i)\psi_0(\mathbf{r}) + a_n(\Omega_i)\psi_n(\mathbf{r})\widetilde{a}_0(\Omega_f)\widetilde{\psi}_0(\mathbf{r})\Big)\frac{1}{\lambda_n-\lambda_0}, \tag{D9}$$

and

$$\alpha(\Omega_i,\Omega_f) \equiv \frac{1}{V}\widetilde{a}_0(\Omega_f)a_0(\Omega_i), \tag{D10}$$

equation (D7) is equation (13) of the text. Note that $\int \Sigma d^3r = 0$, because Σ involves only the product of orthogonal functions. Thus Σ represents an internal redistribution of the asymptotic path density within the ocean and not any net change in the total mass of fluid elements tracing out surface-to-surface paths of a given τ. Consequently, the asymptotic transport-volume and flux-density distributions, $\mathcal{R}$ and ϕ, are determined entirely by the amplitude of the DNP pattern, Ψ. From (6) and (9), $\mathcal{R}$ and ϕ are proportional to the volume integral of η to which Σ does not contribute. As $\tau \rightarrow \infty$, we therefore have $\mathcal{R} \rightarrow \mathcal{R}_\infty$, with

$$\mathcal{R}_\infty(\tau,\Omega_i,\Omega_f) = \frac{1}{V}a_0(\Omega_i)\widetilde{a}_0(\Omega_f)e^{-\lambda_0\tau}\tau, \tag{D11}$$

where we used $\int \Psi\, d^3r = 1$. Correspondingly, as $\tau \rightarrow \infty$, we have $\phi \rightarrow \phi_\infty$, with $\phi_\infty = M\mathcal{R}_\infty/\tau$.

[67] **Acknowledgments.** This work was supported by NSF grants ATM-04-32514 (MH) and OCE-0225156, ATM-0231380 (FP), as well as by NOAA grant NA04OAR4310118 (MH).

References

Albaréde, F. (2003), *Geochemistry: An Introduction*, 248 pp., Cambridge Univ. Press, New York.

Amestoy, P. R., I. S. Duff, J. Koster, and J.-Y. L'Excellent (2001), A fully asynchronous multifrontal solver using distributed dynamic scheduling, *SIAM J. Matrix Anal. Appl.*, *3*, 15–41.

Bradley, R. S. (1999), *Paleoclimatology: Reconstructing Climates of the Quaternary*, 613 pp., Elsevier, New York.

Broecker, W. S. (1991), The great conveyor belt, *Oceanography*, *4*, 79–89.

Broecker, W. S., and T.-H. Peng (1982), Tracers in the sea, pp. 690, Lamont-Doherty Geological Observatory, Palisades, NY.

Colling, A., and Open University Course Team (2004), *Ocean Circulation*, 2nd ed., 286 pp., Elsevier, New York.

Drijfhout, S. S., E. Maier-Reimer, and U. Mikolajewicz (1996), Tracing the conveyor belt in the Hamburg large-scale geostrophic ocean general circulation model, *J. Geophys. Res.*, *101*, 22,563–22,575.

Drijfhout, S. S., P. de Vries, K. Döös, and A. C. Coward (2003), Impact of eddy-induced transport on the Lagrangian structure of the upper branch of the thermohaline circulation, *J. Phys. Oceanogr.*, *33*, 2141–2155.

England, M., and E. Maier-Reimer (2001), Using chemical tracers to assess ocean models, *Rev. Geophys.*, *39*, 29–70.

Ganachaud, A., and C. Wunsch (2000), Improved estimates of global ocean circulation, heat transport and mixing from hydrographic data, *Nature*, *408*, 453–457.

Gent, P. R., and J. C. McWilliams (1990), Isopycnal mixing in ocean circulation models, *J. Phys. Oceanogr.*, *20*, 150–155.

Haine, T. W. N., and T. M. Hall (2002), A generalized transport theory: Water-mass composition and age, *J. Phys. Oceanogr.*, *32*, 1932–1946.

Hall, T. M., and M. Holzer (2003), Advective-diffusive mass flux and implications for stratosphere-troposphere exchange, *Geophys. Res. Lett.*, *30*(5), 1222, doi:10.1029/2002GL016419.

Hall, T. M., T. W. N. Haine, M. Holzer, D. A. LeBel, F. Terenzi, and D. W. Waugh (2007), Ventilation rates estimated from tracers in the presence of mixing, *J. Phys. Oceanogr.*, *37*, 2599–2611, doi:10.1175/2006JPO3471.1.

Holzer, M., and T. M. Hall (2000), Transit-time and tracer-age distributions in geophysical flows, *J. Atmos. Sci.*, *57*, 3539–3558.

Holzer, M., and F. W. Primeau (2006), The diffusive ocean conveyor, *Geophys. Res. Lett.*, *33*, L14618, doi:10.1029/2006GL026232.

Jenkins, W. J. (1988), The use of anthropogenic tritium and helium-3 to study subtropical gyre ventilation and circulation, *Phil. Trans. R. Soc. Lond. A*, *325*, 43–61.

Large, W. G., J. C. McWilliams, and S. C. Doney (1994), Oceanic vertical mixing: A review and a model with a nonlocal boundary layer parameterization, *Rev. Geophys.*, *32*, 363–403.

Lehoucq, R. B., D. C. Sorensen, and C. Yang (1998), ARPACK Users' Guide: Solution of Large-Scale Eigenvalue Problems with Implicitly Restarted Arnoldi Methods, SIAM Publications, Philadelphia.

Marotzke, J. (1997), Boundary mixing and the dynamics of three-dimensional thermohaline circulations, *J. Phys. Oceanogr.*, *27*, 1713–1728.

Matsumoto, K., and R. M. Key (2004), Natural radiocarbon distribution in the deep ocean, in *Global Environmental Change in the Ocean and on Land*, edited by M. Shiyomi et al., pp. 45–58, TERRAPUB, Tokyo.

Morse, P. M., and H. Feshbach (1953), *Methods of theoretical physics*, McGraw-Hill, 997 pp.

Munk, W., and C. Wunsch (1998), Abyssal recipes II: Energetics of tidal and wind mixing, *Deep-Sea Research I*, *45*, 1977–2010.

Orsi, A. H., S. S. Jacobs, A. L. Gordon, and M. Visbeck (2001), Cooling and ventilating the abyssal ocean, *Geophys. Res. Lett.*, *28*, 2923–2926.

Pacanowski, R. C., K. Dixon, and A. Rosati (1993), The GFDL modular ocean model users guide, GFDL Ocean Group Tech. Rep. No. 2, GFDL, Princeton.

Primeau, F. (2005), Characterizing transport between the surface mixed layer and the ocean interior with a forward and adjoint global ocean transport model, *J. Phys. Oceanogr.*, *35*, 545–564.

Primeau, F., and M. Holzer (2006), The oceans memory of the atmosphere: Water-mass residence-time and ventilation-rate distributions, *J. Phys. Oceanogr.*, *36*, 1439–1456.

Robbins, P. E., J. F. Price, W. B. Owens, and W. J. Jenkins (2000), The importance of lateral diffusion for the ventilation of the lower thermocline in the subtropical North Atlantic, *J. Phys. Oceanogr.*, *30*, 67–89.

Schmitz, W. J. (1995), On the interbasin-scale thermohaline circulation, *Rev. Geophys.*, *33*, 151–173.

Sidje, R. B. (1998), Expokit: A software package for computing matrix exponentials, *ACM Trans. Math. Software*, *24*, 130–156.

Speich, S., B. Blanke, and G. Madec (2001), Warm and cold water routes of an O.G.C.M. thermohaline Conveyor Belt, *Geophys. Res. Lett.*, *28*, 311–314.

Sun, S., and R. Bleck (2001), Thermohaline circulation studies with an isopycnic coordinate ocean model, *J. Phys. Oceanogr.*, *31*, 2761–2782.

Toggweiler, J. R., and B. Samuels (1993), New radiocarbon constraints on the upwelling of abyssal water to the ocean's surface, in *The Global Carbon Cycle*, *NATO ASI Ser. I*, *Global Environ. Change*, edited by M. Heinmann, pp. 333–366, Springer Verlag, New York.

Toggweiler, J. R., and B. Samuels (1998), On the ocean's large scale circulation in the limit of no vertical mixing, *J. Phys. Oceanogr.*, *31*, 3121–3126.

Toole, J. M., K. L. Polzin, and R. W. Schmitt (1994), Estimates of diapycnal mixing in the abyssal ocean, *Science*, *264*, 1120–1123.

Waugh, D. W., T. W. N. Haine, and T. M. Hall (2004), Transport times and anthropogenic carbon in the subpolar North Atlantic Ocean, *Deep-Sea Res. I*, *51*, 1475–1491.

M. Holzer, NASA Goddard Institute for Space Studies, 2880 Broadway, New York, NY 10025, USA. (hm2220@columbia.edu)

F. Primeau, Department of Earth System Science, University of California, 3216 Croul Hall, Irvine, CA 92697-3100, USA. (fprimeau@uci.edu)